Spring 2019

Friction Stir Additive Manufacturing(FSAM) of 2050 Al-Cu-Li Alloy

Ilana Lu

FRICTION STIR ADDITIVE MANUFACTURING (FSAM) OF 2050 AL-CU-LI ALLOY

by

Ilana Lu

Bachelor of Science
University of South Carolina, 2017

Submitted in Partial Fulfillment of the Requirements

For the Degree of Master of Science in

Mechanical Engineering

College of Engineering and Computing

University of South Carolina

2019

Accepted by:

Anthony Reynolds, Director of Thesis

Addis Kidane, Reader

Cheryl L. Addy, Vice Provost and Dean of the Graduate School

DEDICATION

This work is dedicated to my mom and brother. I could not have made it this far without your unwavering support.

ACKNOWLEDGEMENTS

Firstly, I'd like to acknowledge my faculty advisor Dr. Tony Reynolds for the opportunity to conduct this research and his guidance during the process. Suffice to say, the education and experience from working with Dr. Reynolds has been transformative.

Special thanks to Dr. Mike Sutton, Dr. Xiao Li, Dr. Dario Baffari, and Mr. Dan Wilhelm for their mentorship and assistance before and during graduate school. I would also like to acknowledge the help of Mr. Addis Tessema for guidance with digital image correlation.

I would finally like to recognize the financial support of the Center for Friction Stir Processing which is a National Science Foundation I/UCRC supported by Grant No. EEC-0437341.

ABSTRACT

As a solid state process, friction stir welding (FSW) is an advantageous joining method for higher strength aluminum alloys such as 2050 Al-Cu-Li which are not readily fusion welded. This study explores the potential of friction stir lap welding (FSLW) as an additive manufacturing process for this aluminum-lithium alloy. To accomplish this, lap weld joints were performed so that each additional layer would penetrate the preceding weld pass which creates a large, stacked build. Excess material is machined away leaving only weld. Cast AA2050 is explored in this study as a more cost-efficient feedstock for this process as compared to wrought plate.

Three builds of 2050 aluminum alloy were studied for weld response variables, and properties. These variations included: (i) 25mm length pin and cast 2050 aluminum alloy in three layers including 2050-T3 substrate and top layers, (ii) 12.85mm length pin and cast 2050 in seven total layers with a 2050-T3 substrate/top, and (iii) 12.85mm length pin and 2050-T3 in all seven layers. A finite element analysis (FEA) was also performed to compare beams made from the AM process and from monolithic 2050 plate.

All builds exhibited inhomogeneous hardness distributions with minimums in the overlapping heat affected zones. In addition to the hardness results, transverse tensile tests of two of the builds showed that strain tended to concentrate in the soft, heat affected zones but overall the builds possess moderately good ductility and weld efficiency. Fracture tests of weld material demonstrated complex behavior—fracture resistance of the welds was higher than that of the parent material; however, the presence

of inhomogeneous hardness and process-created distributions added a level of irregularity. Overall, it was found that there is not a disadvantage to using cast material in friction stir additive manufacturing (FSAM) however the practicality of this process is not ideal at the current technology level.

TABLE OF CONTENTS

LIST OF TABLES

LIST OF FIGURES

CHAPTER 1

INTRODUCTION

1.1 Motivation for Study

Additive manufacturing is a presently growing industry with applications now focusing on metallic materials and processes intended to reduce waste and cost of fabricated parts. Friction stir welding is a well-established method of solid state material joining which additionally can also be applied to process materials microstructurally. An amalgamation of these different technologies, the governing motivation for this study includes examining the method of friction stir lap welds for their potential as an additive manufacturing process for high strength aluminum alloys such as AA2050. In addition, it will be determined if cast AA2050 can be used for friction stir additive manufacturing as a less costly alternative to its wrought counterpart.

1.2 Friction Stir Welding Overview

As it was only developed within the last few decades, friction stir welding (FSW) is considered a relatively new technology but extensive testing proves its maturity and effectiveness of joining materials [1-2]. It is a solid state process, meaning material should never reaches bulk melting temperature but instead is joined through intense plastic deformation and pressure from the tooling. This is especially useful for heat treatable aluminum alloys that are not typically fusion welded due to a loss in strength from the dissolution of precipitates—Particularly high strength es from the 2XXX and 7XXX

aluminum alloy families [2]. Shown in the schematic of Fig. 1.1 below, this process involves a nonconsumable rotating pin which is applied to the work piece with forging force and then travels on a designated path.

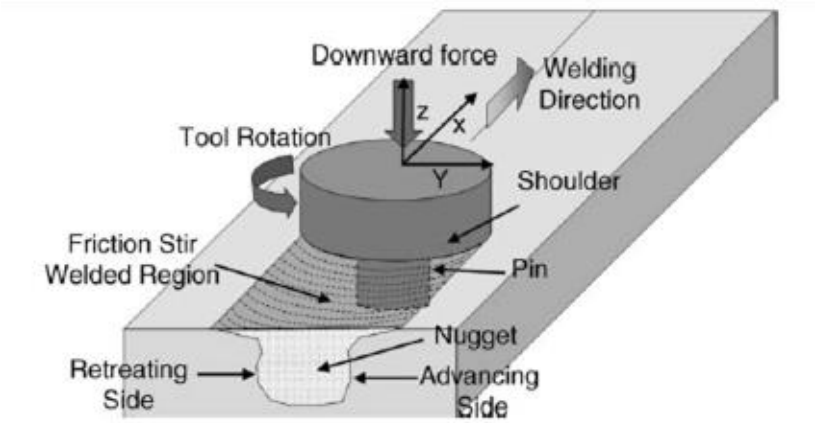

Figure 1.1 Illustration of the FSW process [1]

Complex material flow occurs as the stirring action induces a vortex of softened material around the probe itself and an elliptical extrusional motion as it attempts to escape and is pushed back into the material from the tool shoulder. As thermal energy is mostly generated from the contact from shoulder tooling and work material, a temperature gradient exists which can lead to microstructural differences throughout the weld [1, 3].

The areas of a friction stir weld are typically divided into several sections to differentiate the properties or thermal/mechanical history as shown in Fig. 1.2. This includes the mechanically unaffected parent material, heat affected zone (HAZ), and the thermo-mechanically affected zone (TMAZ) also known as the stir zone (SZ) or nugget material. Equiaxed grains are formed within the nugget through dynamic recrystallization (DRX) resulting from high strain rates and temperature. These recrystallized grains contribute to optimized mechanical properties [1-2, 4].

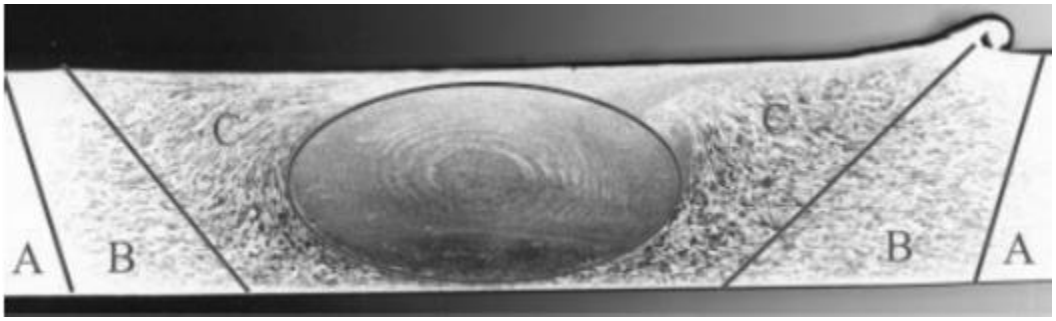

Figure 1.2 Cross-sectional view of a friction stir weld and its zones: (A) Unaffected parent material, (B) the heat affected zone (HAZ), and (C) thermomechanically affected zone (TMAZ) with weld nugget encircled [2]

1.3 Friction Stir Additive Manufacturing

Similar to fusion welding, industry-relevant additive manufacturing methods such as direct energy deposition (DED) are prone to cracking, porosity, anisotropy, and residual stress due to the temperature of the processes [5]. In addition, materials that are difficult to weld with fusion methods such as 2XXX series aluminum alloys are also obviously not ideal for DED additive processes.

Applications of friction stir processing are used in several additive manufacturing technologies such as the introduction and processing of powder through the tooling, bonding of layers of cladding or feedstock, and functionally gradient materials (FGM) among other concepts. An immediate benefit of the additive manufacturing concept is a reduced buy-to-fly ratio of components such as those used in the aerospace industry—current methods of producing complex geometry include machining of large wrought billets which results in a large amount of wasted material [6]. FSAM also offers the benefits of additively manufacturing the aluminum alloys difficult to weld traditionally.

The aforementioned FSW through layers of cladding can be implemented with a conventional gantry friction stir welding machine needing no additional modifications. It

also has potential for thicker layers and complex geometry depending on the CNC capability of the machine. A demonstrator using FSAM lap weld cladding technique can be seen in Figures 1.3 and 1.4 courtesy of the Edison Welding Institute (EWI) [7].

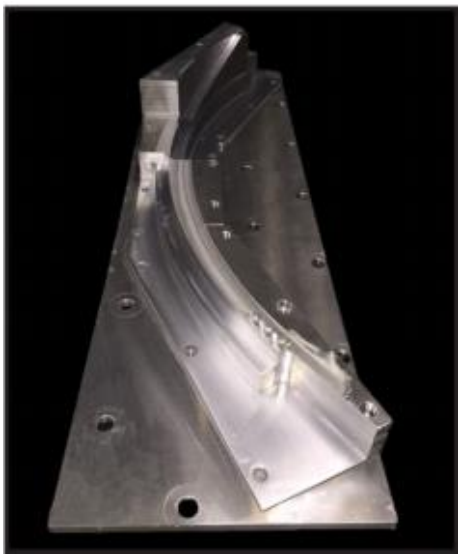

Figure 1.3 EWI FSAM demonstrator with the cladding method [7]

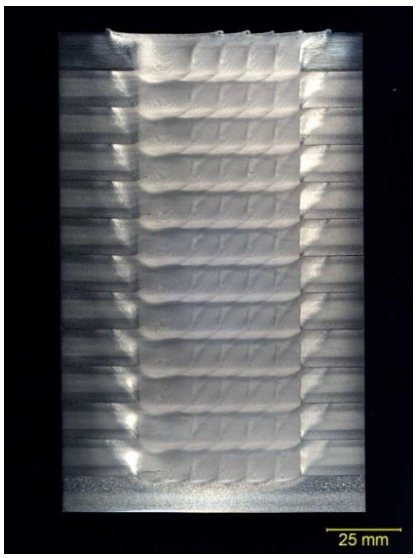

Figure 1.4 Cross-sectional view of FSAM [7]

A similar practical application of this process is shown in Figure 1.5 on the next page where feedstock material is placed on a substrate and lap welded, penetrating through the plate thickness. This process is continued until the user has completed the build with a top layer of the chosen temper of material. Excess material is machined from the lap weld builds leaving mostly processed weld nugget with sections of HAZ interspersed throughout. The dimension of the final design is dependent on the weld width, *W*, and plate thickness *T*. Preliminary studies regarding this method of AM identify integrally stiffened panels and stringers as the target industry geometry for this process [8].

This friction stir additive manufacturing method method implements lap weld joints instead of a more traditional butt joint, the difference illustrated in Figure 1.6. The main distinction between the two configurations is the direction of the interface relative to the weld tool rotation axis: butt joints have vertical interfaces which align with the rotational axis. However, lap joints implement a horizontal interface which is perpendicular to the tool rotational axis [9]. Characteristics relevant to this configuration are discussed in the succeeding section.

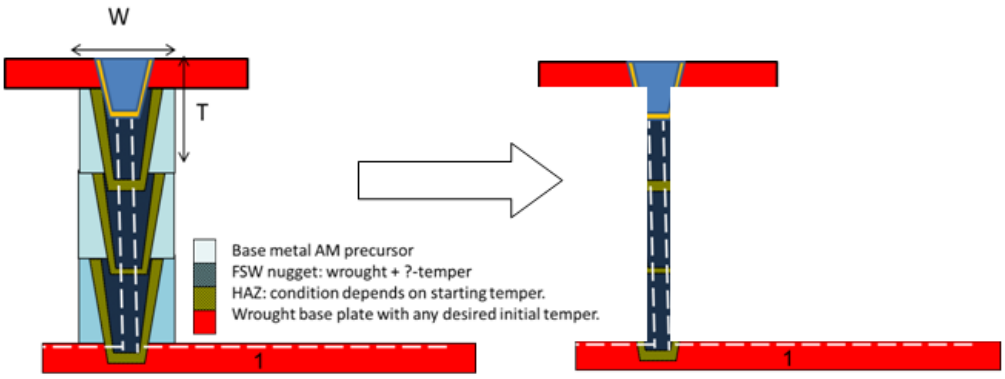

Figure 1.5 Schematic of FSAM with lap welds

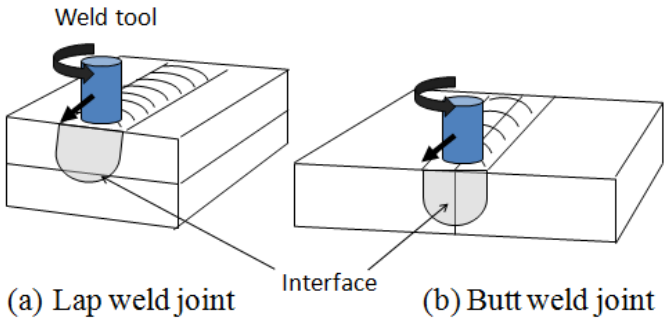

Figure 1.6 Comparison between butt and lap joints with FSW

1.4 Lap Welding Overview

1.4.1 Lap Weld Defects

Widely found in studies of this weld configuration, metallographical analysis of lap weld cross sections may exhibit unbonded, crack-like characteristics related to the ineffective destruction of the original interface. The profiles of the features can be of a variety of shapes, depending on parameters or other conditions. These defects appear differently on either side perpendicular to the weld travel line as the material flow is asymmetrical in nature [10-12]. Referred to as hooking and cold lap defect, an illustration of these is in a lap weld is shown in Figure 1.7.

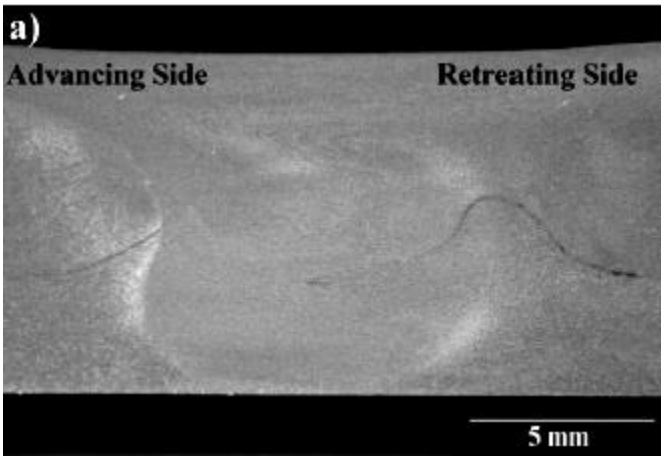

Figure 1.7 Hooking shown on advancing side and retreating CLD [13]

On the advancing side, the hook defect (HD) tends to flare upwards. On the retreating side, the residual undestroyed interface can stretch into the stir zone itself while also shifting upwards from the nominal interface and has been referred to as "plate thinning", "cold lap defect (CLD)", or even "remnant joint line" [9, 12-15]. The CLD has been shown to exhibit anywhere from a smooth contour to that of a jagged sawtooth profile. The vertical displacement of the CLD is attributed to extrusional action from the tooling

combined with thermal conditions [12]. Cederqvist et al. defined the phrase "effective sheet thickness (EST)" which assists in quantifying the severity of the CLD defect, as the height deviation from the nominal interface location determines the amount of weld nugget available to be burdened mechanically and has noticeable effects on the failure load especially when sheared. The consensus among studies in this area concluded that when considering shear-tensile tests, hook orientation affects the potential strength as the defect can act as an existing crack from which to propagate [9, 12, 14, 16].

1.4.2 Tool Geometry

As compared to a cylindrical pin, a tapered tool was shown to provide better vertical flow for lap welds [9]. Babu et al. also established that well-performing lap welds were performed with a threaded tapered pin when compared to a triangular tool and the traditional joining method of riveting [11]. The pin geometry induced a downward vertical material flow to increase the EST of the cold lap defect. It was also observed by Aldanondo et al. that a threaded tool containing three flats offered better consolidation and nugget size for lap welds [17].

Regarding probe length, Cederqvist et al. demonstrated that out of three tools of different length the longer pin contributed to a vertical displacement of the residual interface while the shortest one caused a downwards vertical feature. The mid-length pin generated a close to nominal interface height [18]. Shoulder and pin tip designs have not been regarded to noticeably affect the weld nugget width, however minimum hardness is found to be in the HAZ near the outer diameter of the shoulder, as has been generally seen with most FSW [18-20]. Welding tools specifically for the lap configuration have been

developed, most notably the trademarked Triflute, Trivex, A-Skew among others [1, 21]. These tools were designed to mitigate lap welding problems but require skilled machining due to the complex geometry and are also trademarked, making their use more expensive due to licensing costs.

1.4.3 Process Parameters

It has been observed that the increase of rotational speed led to the increase of vertical flow, therefore reducing the EST [13]. However, the increase of weld travel speed in many different metallic alloys was shown to reduce defect features and decrease the retreating side interface height as the upwards vertical flow was lessened [13,16,20, 23]. Likely due to this mitigation of the cold lap internal defect, increase of weld travel speed was also shown to directly improve shear-tensile results of lap welds [12-13]. At a certain point of increased travel speed, however, advancing side cavity defects were noted to appear in aluminum alloy studies as the material required additional heat generation to plastically deform. Considering combinations of process parameters, a "colder" weld, or one that has a higher ratio of welding travel speed to tool rotational speed, has been shown to increase the effective sheet thickness [12, 16, 18].

1.4.4 Weld Strategy

Demonstrated by Cederqvist *et al*., an effective plan to control lap weld sheet thickness was to implement a double pass welding strategy. This was done by performing a second weld at the opposing weld direction of the first but indexed on the advancing side of the first weld. The resulting weld contained two retreating sides and both advancing

sides encapsulated in the stir zone. This was subsequently verified by Dubourg *et al.* who observed that the double pass method indeed resulted in a much stronger weld when compared to that of a single pass [22]. In both of the major studies, welds performed with a double pass showed higher load strength likely due to the elimination of sharp stress areas like the advancing side hook as compared to similar single weld counterparts. The double pass strategy is beneficial when considering an additive manufacturing model with lap joints—elimination of the insufficiently bonded interface results in usable nugget.

1.4.5 Kissing Bond

Authors of previous investigations found these defects at the locations in the retreating side of the stir zone, which resulted from remnants of surface oxides from the welding process [13, 16]. It was observed that a faster advancing speed resulted in a kissing bond in lap welds, which correlates to previous findings with butt weld kissing bond formation [2]. This is due an overall lower welding temperature and the orientation of the interface with respect to the pin, resulting in an inadequately disrupted oxide from the faying surfaces—so in this instance, a hotter weld is more appropriate to eliminate this defect [13, 15-16].

1.4.6 Lap Welding Summary

From accounts of previous studies with lap welding, the defects common to this configuration have been shown to be reduced by taking precautionary process development steps. These include the tool geometry, process parameters, and a weld strategy. Defects such as the crack-like cold lap on the retreating side, severe advancing side hooking, or

near-invisible kissing bonds reduce the strength of the welds and steps should be taken to prevent them from forming. An ideal lap weld for FSAM is one that has a large nugget width achieved from the management of CLD. However, from the many previous studies, there is shown a balance between process parameters and tool geometry needed to achieve a weld that is not only fully consolidated but also has minimized lap defects. It has been recommended to consider the design allowables depending on the application of FSLW to prepare for the possibility of defects [24]. With FSAM, the excess material is intended to be machined away so the major concerning defect is that of the cold lap of the retreating side.

In general, much has been studied about friction stir lap welding characteristics, but little is known about the application of it for additive manufacturing. The succeeding sections will explore the use of FSLW as an additive manufacturing process through examining the mechanical properties of large-scale builds. Tensile testing using digital image correlation (DIC) and fracture testing with CT specimens has not been done for FSLW studies in the past, and can reveal more about the potential for this technology process.

1.5 AA2050 Metallurgy

The third-generation aluminum alloy of 2050 Airware© was designed relatively recently for structural aerospace applications. Its chemical composition is displayed in Table 1.1 on the next page.

Table 1.1 Chemical composition of AA2050 [25]

Wt %	Si	Fe	Cu	Mn	Mg	Zn	Li	Ag	Zr
Min			3.2	0.20	0.20		0.70	0.20	0.06
Max	0.08	0.10	3.9	0.50	0.60	0.25	1.3	0.7	0.14

As lithium is the lightest of the metallic elements, an immediate benefit of this alloy includes reduced density—up to 5% when compared to legacy alloy 7050-T7 [25, 26]. Beneficial characteristics of this alloy include high strength, resistance to stress corrosion cracking and good toughness. This Al-Cu-Li alloy's mechanical performance compares easily to current industry alloys 7050 and 2024, overtaking the latter. However, the price to develop 2050 is not insignificant due to additions of elements such as lithium and silver which are highly reactive and precious metal respectively.

In monolithic form, the best-performing AA2050 is that of T8 temper which is subject to solution heat treating, cold work, and artificial aging. Solution heat treating temperature for similar alloys is between 500 and 530˚C, while the artificial aging for peak performance is in the range between 130-170˚C for at least 15 hours [27-28]. Vickers pyramid hardness of AA2050-T8 material was measured in the range of 170-180 HV within previous studies and laboratory analysis [28-30]. Various investigations also attribute yield strength to be between 490-520 MPa. Ultimate tensile strength was experienced between 540 and 590 MPa with total elongation of 8-13 percent [29, 31-32].

The 2050-T3 temper is also solution heat treated and cold worked but allowed to age naturally. Sometimes referred to as the "underaged" state, the mechanical strength of this condition is less than that of the T8—Yield strength of this temper was found in the ranges of 243-295 MPa, while the UTS were shown to vary from 376-470 MPa [29, 33].

However, maximum elongation of the underaged stage was established to be 14-22%. Hardness of T3 material has shown to range between 120-130 HV.

Unlike wrought designations, the cast aluminum alloy of the 2050 composition referred to in succeeding sections as one of the feedstock materials has been subject to a homogenization treatment to improve the chill-casted dendritic structure. Recommended temperatures for these kinetics in similar alloys are held between 480˚C and 512˚C for 5 to 60 hours [27-28]. Lab measured Vickers hardness of cast 2050 material is approximately 80 HV.

Containing lithium, AA2050 is primarily strengthened through the T_1 phase (Al_2CuLi) which precipitates as platelets, distributed homogeneously with an affinity for dislocation sites [25, 34]. Other observed phases within the base metal alloy are those of θ' and S'. Microstructural characterization of a friction stir weld from T3 base material and subject to a post-welding aging showed reduction in the density of the T_1 phase through the weld depth which accompanied a reduction in hardness from the near-shoulder top to pin bottom [35]. In addition, notable heterogeneity of microstructure has also been noticed in previous analyses of thick FSW joints involving this alloy [29-30, 37-38].

CHAPTER 2

EQUIPMENT AND PROCESS

2.1 Material Preparation

Plates of cast and AA2050, AA2050-T8, and AA2050-T3 were received in large blocks and cut with a band saw to a size close to the final nominal size of 432 mm in length and 102 mm wide. For the large build, plates were milled to a thickness of 23 mm while the smaller pin required plate thicknesses of 12 mm. It is important to note that as the three materials were received at different periods and from various distributors, the compositions may have varied from each other but are assumed to be within the acceptable range for this alloy.

After a light flycut with a milling machine to ensure flatness, edges were deburred with a file. A hole was drilled at the plunge locations for each weld using bits that were close to the dimensions of the welding pins.

2.2 Tool Geometry

For the three separate builds, two tools and shoulder sets were used. Both pins were fabricated from MP159 material and their specifics for geometric features are displayed in Table 2.1 and also shown in Fig. 2.1. Detailed CAD drawings for the tools and shoulders are shown in Appendices A and B. For identification purposes within this study, the larger pin is referred to as the 25 mm pin, and the smaller tool as the 12.85 mm pin. The shoulder geometries for these corresponding pins are also given in the table.

Both shoulders were made from H13 tool steel with a 1.6 APR single lead scroll. The depth of the scroll was at 1 millimeter with the feature machined to a 3.18 mm ball end mill.

Table 2.1 FSW pin tool geometric properties

Pin length, mm	**25**	**12.85**
Thread pitch, thread/mm	1.75	1.5
Largest diameter, mm	19.1	12.7
Smallest diameter, mm	8.9	8.26
Taper, degrees	8	10
Number of flats	3	3
Flat depth, mm	0.89	0.76
Shoulder diameter, mm	35.6	28.6

Figure 2.1 Both pins used for the FSLW builds

2.3 Thermal Management

An O1 tool steel backing plate of 8 mm thickness was used under the builds, and trailing water spray applied to the welding as an active cooling method. The fluid was applied at a rate of 0.45 liters per minute.

2.4 Welding Procedure

The FSW Process Development System (PDS) machine used for this study was developed and fabricated by MTS Systems Corporation for the University of South Carolina. Shown in Figure 2.2, it is capable of up to 133 kN in the z-axis direction (plunge) and up to 67 kN in the x-direction (weld travel). The torque capacity is up to 678 N-m with a 5-to-1 gear reduction fitted to the system.

Figure 2.2 Friction stir welding PDS

Prior to welding, the substrate sheet was placed on the backing plate and then the first layer was added and clamped down on both sides of the weld travel line, demonstrated in Fig. 2.3. The first pass was then welded at the designated offset of tool center to build centerline. Manual alignment of the welds was performed to index them to the correct locations. The second weld pass of each layer was performed in the opposing travel direct of the first, however with the advancing sides overlapped at a specified amount using an "offset" metric, as defined in Fig. 2.4 with a cross sectional schematic. This is simply the distance of the tool center for each weld pass to the datum center line of the weld build.

Fig 2.3 Plates clamped in fixture

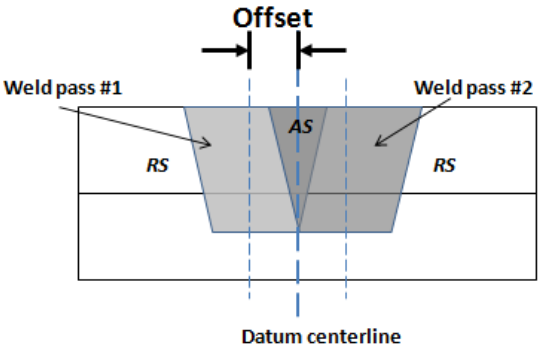

Fig 2.4 Defining offset of the double weld passes

After the double weld pass was completed, the weld build was removed from the clamps and smoothed on a mill to ensure a flat interface for the succeeding layer. It would then be replaced in the weld machine and clamped again to the appropriate indexing locations. Welded layers could then be added with this iterative process until the desired height was reached. It is important to note that the final height of the builds within this study was equivalent.

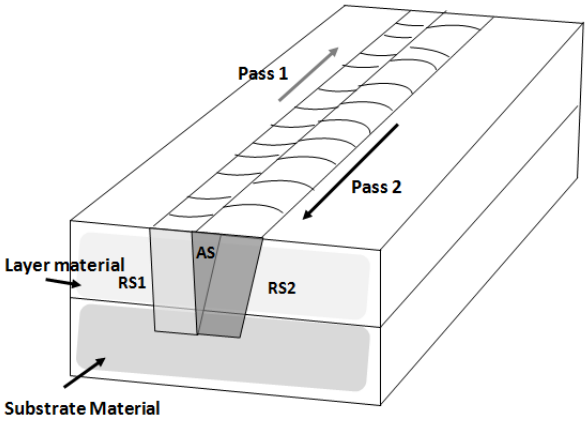

Fig 2.5 First layer of FSAM process

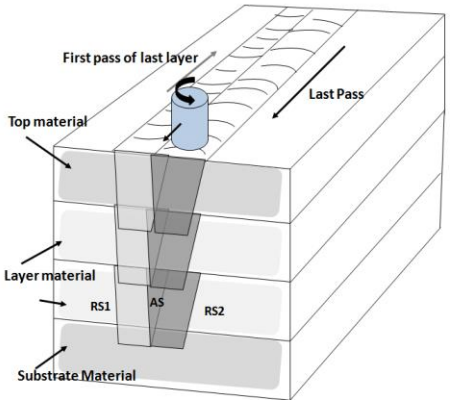

Fig 2.6 Layer iterations

All three builds were intended to be constructed in the above manner; however, they differ in the lapping sequence and configuration as shown in Table 2.2. It is important to note that the thinner, faster T3 build was welded incorrectly, as the plates were rotated in the wrong direction, resulting in two advancing sides on the outside of the welds instead of the retreating-retreating double pass.

Table 2.2 Final builds: pin type, plate thicknesses, and lapping sequence

Build	***Slower/thicker/cast***	***Faster/thinner/cast***	***Faster/thinner/T3***
Pin length, mm	25 mm	12.85 mm	12.85 mm
Plate thickness, mm	23	12	12
Offset, mm	3.18	1.91	1.91
Layer material	Cast	Cast	T3
Substrate and top material	T3	T3	T3
Number of lap layers	4	7	7

2.5 Weld Process Parameters

Process parameters for the builds were determined after initial trials with pins and additional material. Basic criteria used to determine working parameters and operating window for each pin was to achieve a fully consolidated weld with a minimum of obvious defects such as excessive flash and wormholes.

Table 2.3 Weld process parameters for all builds

Build	***Slower/thicker cast***	***Faster/thinner/cast***	***Faster/thinner/T3***
Commanded RPM, counterclockwise	200	250	250
Commanded travel speed, mm/min (*in/min*)	152.4 (*6*)	203.2 (*8*)	203.2 (*8*)
Commanded plunge force, kN (lb_f)	53.38 (*12,000*)	31.14 (*7,000*)	33.36 (*7,500*)
Tilt angle, degrees	1	1	1

2.6 Data Acquisition and Response Variables

K-type thermocouples were embedded at the midplane of both pins to collect data on the thermal conditions welds experienced during the process. Information was synced wirelessly to a standalone laptop through the use of a TC-Link® lossless thermocouple node. Torque information was noted through Datum Electronics torque transducer and, and documented to the Torquelog program. Weld response variables of the in-plane forces were automatically logged with the welding machine PDS.

2.7 Post-Weld Heat Treatment

Builds were aged naturally for at least two weeks after the welding process. For the post-welding heat treatment, samples were treated in an oil bath at 160˚C for 15 hours as a treatment intended to age T3 material to mechanical performance of T8 temper as per recommendations for this alloy and other similar aluminum alloys [27-29, 33].

2.8 Metallographic Samples and Analysis

Samples from the builds were sliced with a vertical bandsaw at least halfway into the weld length for a steady-state analysis. They were then hand ground with silicon carbide sand paper from 120 - 1200 grit. Once the finish was evenly smooth at the final grinding stage, a polish was applied with alumina powder of 5 micron diameter and then 3 micron using a soft polishing cloth. Colloidal silica suspension of 0.06 μm was finally used as a final chemical polishing step. To visibly reveal microstructure, Keller's reagent was mixed using 190 mL water (H_2O), 5 mL nitric acid (HNO_3), 3 mL hydrochloric acid (HCl), and 2 mL hydrofluoric acid (HF) in the stated order from least reactive to most reactive. Samples were placed into the solution for 10 seconds then rinsed with fresh water and thoroughly dried with compressed air. Removal of debris, dust, and oil on samples used denatured alcohol and a cotton swab.

Macrographical observation and image capture was performed on a VHX-5000 series digital microscope. Samples were examined for any obvious flaws and lap welding features. Cross-sectional images too large to be stitched with microscopy were taken with a Canon LiDE 110 digital scanner.

2.9 Hardness Testing

A Buehler Micromet 1 hardness testing machine was used to perform Vicker's microhardness analysis. A load of 200 grams-force was used for all samples with a dwell time of 10 seconds. Indents were spaced apart at either a distance of 317.5 microns or double of 635 microns depending on the density needed in the sample. The amount of hardness indents for each sample varies, as the analysis is performed from the welded areas until parent material hardness is reached.

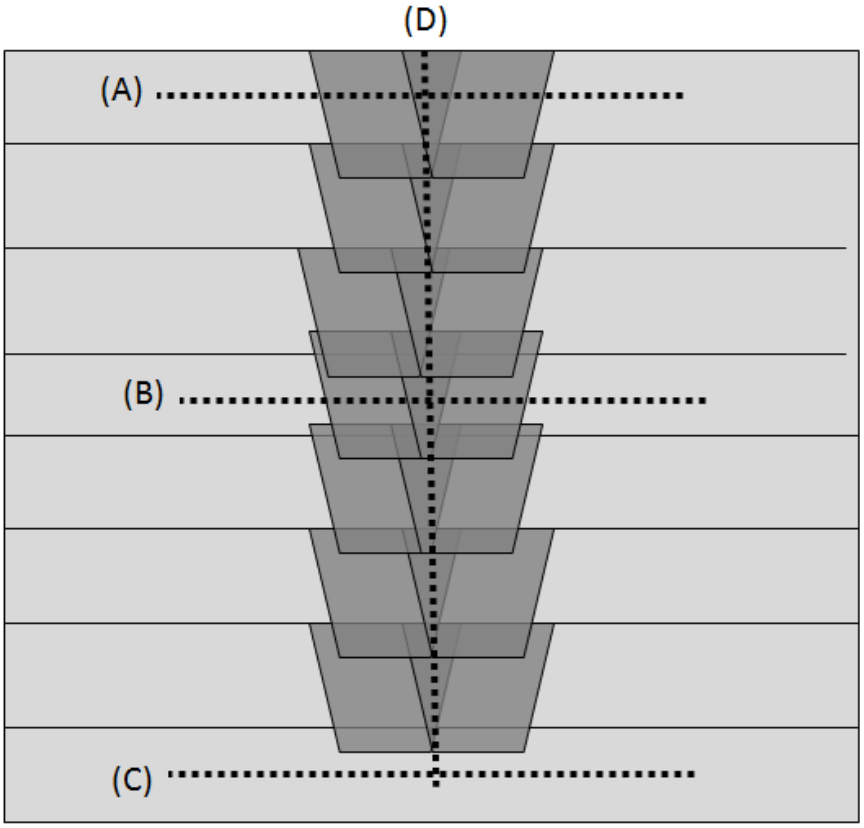

Fig. 2.7 Hardness testing positions within lap weld layers

Vickers hardness analysis was performed on all base metal samples to quantify the parent material properties. For welds, testing was conducted in the as-welded condition then again after the applied heat treatment. Hardness measurements were taken at pin midplanes of the top (A), bottom (C), and centermost (B) layers of each build as indicated

in the cross-sectional weld illustration of Figure 2.7. However, build 4771 did not have this performed on segment (C). The analysis was also performed at (D) at the weld centerline through the layer thicknesses for all builds.

The formula used to calculate the resulting Vickers Pyramid Hardness Number (VHN) for the analysis is given in Equation 2.1.

$$HV = 1854\left(\frac{F}{d^2}\right) \qquad (Eq.2.1)$$

Where the hardness number, HV (kg_f/mm^2) depends on the indentation force, F (g), and mean diameter of the diamond-shaped indentation, d (μm).

2.10 Digital Image Correlation Tensile Testing

Transverse tensile test specimens were machined from the weld material in the layout shown in Fig. 2.8 on the next page. Sample geometry is given in Appendix C. Tensile specimens were cute to extend the height of the builds to include as many layers as possible. The uniaxial tester used for these specimens was a MTS Exceed E43 with a capacity of 30 kN. For all specimens, the strain rate was set to 0.0254 millimeters per second (0.001 inches per second). Where possible, heat treated samples from each build were also tested to compare with their as-welded counterparts.

Digital image correlation (DIC) was performed by initially speckling the samples with a uniformly fine and random pattern using a black spray paint on a white base. An example of the dogbone tensile specimens with this sprayed pattern is shown in Figure 2.9 on the next page. High resolution pictures were taken every second while axially loaded to capture deformation with a 5-megapixel camera equipped with a 100 mm lens. The complete setup is shown in Figure 2.10. Corresponding load voltage was logged for every

image through an analog output from the testing system. Given the capacity of the machine, the conversion factor of 3kN per 1V of load was established and used to analyze the load data. Post processing of the DIC tensile data was performed using Correlated Solutions VIC 2-D 2009 software.

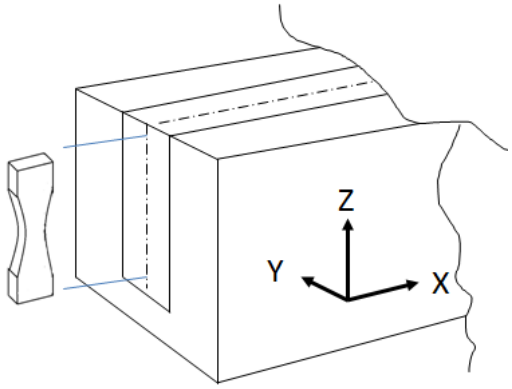

Fig. 2.8 Orientation of tensile specimens within the weld material

Fig. 2.9 Speckled pattern on DIC tensile samples

The Extensometer feature of VIC 2-D was used on the area of interest (AOI) of samples to determine values for the stress-strain curve. This feature allows the average strain for this area to be calculated like that of a conventional extensometer applied to a tensile sample. Local strain values were also calculated for samples with the correlation software.

Fig. 2.10 Tensile DIC equipment setup

2.11 Fracture Testing

Compact tension (CT) specimens for fracture testing were machined as per the ASTM E1820 standard for fracture toughness [38]. The specimen dimensions are given in Appendix D. In order to test purely weld material, samples were machined to a thickness of 7 millimeters. Samples of monolithic 2050-T8 material in the S-T rolling direction were

also machined with identical geometry. Several configurations of crack growth orientation were used for each build to explore crack growth behavior: (1) from bottom to top of build, (2) growing in opposite direction of last pass weld travel, (3) from top to bottom of build, and (4) growth in the direction of weld travel. This is also given in Table 2.4 and can be observed in Figure 2.11. All fracture specimens apart from the base T8 material were given the preceding heat treatment method.

Table 2.4 Orientations of crack growth in samples

Sample designation	Orientation of crack growth
1	Bottom to top direction of builds
2	Opposite welding direction at approximate build midplane
3	Growing from top to bottom of builds
4	With welding direction at approximate build midplane

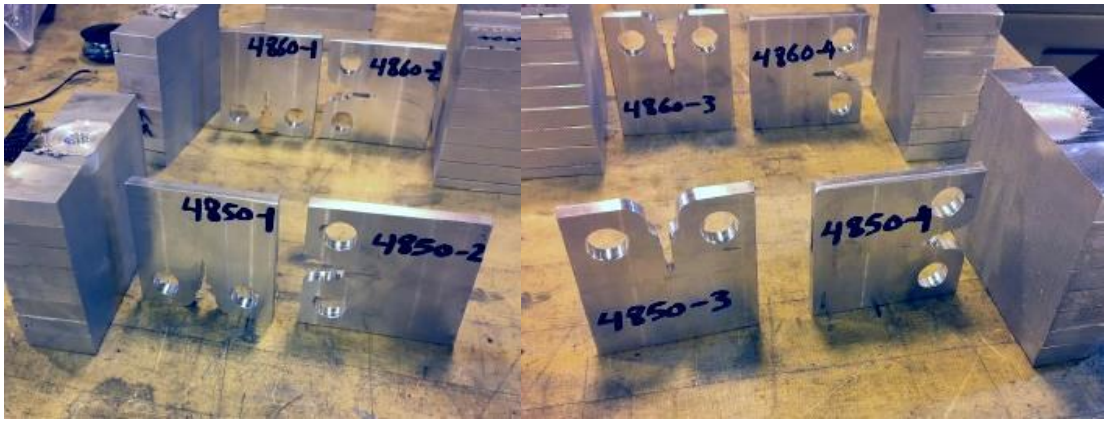

Figure 2.11 Machined C-T specimens with notch orientations for crack growth

An MTS-810 servo-hydraulic materials testing system with a force range up to 100 kN was used to grow a fatigue crack in each sample according to ASTM E647 with the assistance of software from Fracture Technology Associates. The drop voltage compliance method was implemented to monitor the crack growth with the use of a gage placed within the knife edge of sample crack openings, such as in Figure 2.11. With an additional program from FTA and the compliance method, the nonlinear fracture toughness was investigated as per ASTM E1820. Post-processing of results with the software suite yields crack growth distance Δa and the calculated fracture toughness, K_{JIC}.

Figure 2.12 Gage for compliance method CTOD

CHAPTER 3

RESULTS AND DISCUSSION

3.1 Weld Process Feedback

For this study x-force feedback is defined as the in-plane forces experienced by the welding tool in the longitudinal welding direction. The other in-plane force is that of the y-force response as the transverse force within the z-direction is responsible for plunge. Analysis for the welding data involved taking running averages of portions identified as steady state operation. This was done for each individual pass of all three builds. A concise comparison view of the normalized build response variables is shown in Figure 3.1 on the next page and full data for each build is shown in Appendix E through Appendix G.

It is expected that the y-axis response force is always higher than that of the weld travel x-axis response force, and this was seen with all these builds. Z-feedback forces correspond closely to the commanded plunge forces which were anticipated values.

Observations of the build layer data in Appendices E-G and that of the generalized summary table indicate that feedstock material properties have an effect on the forces experienced during this process. Specifically, the thinner/faster T3 build and any layers from the two other builds containing 2050-T3 material experienced greater

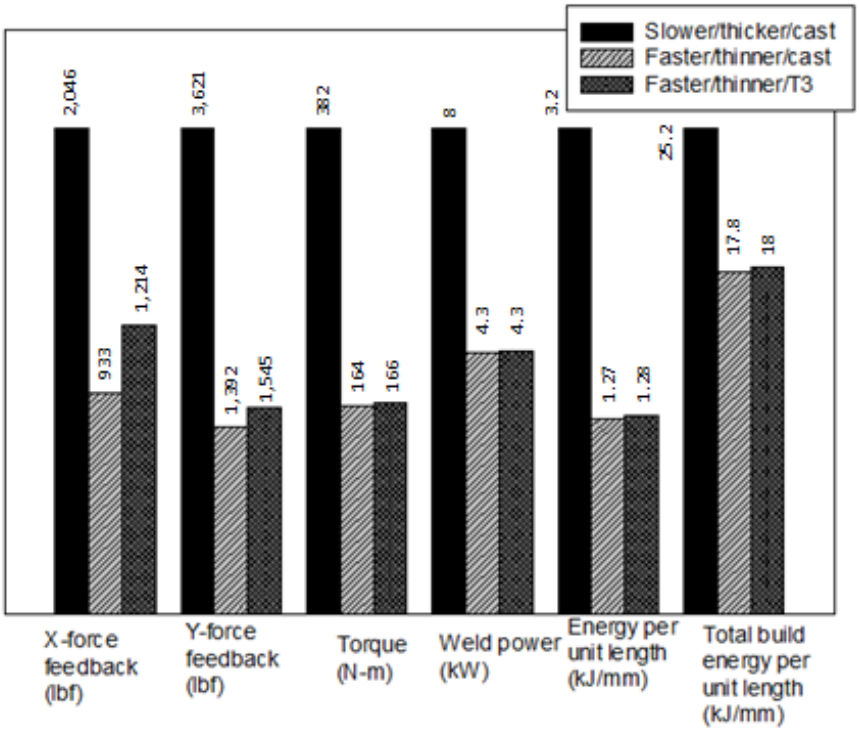

Figure 3.1 Comparison of all three build average response variables

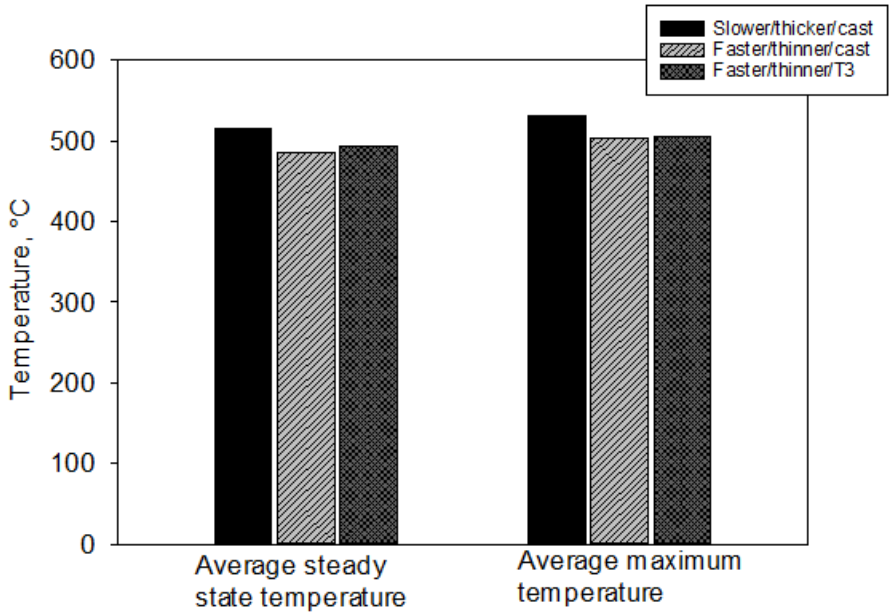

Figure 3.2 Build temperature responses

forces, increased temperatures, and required a larger plunging force. However, second passes of T3 plates showed a decrease in in-plane forces and temperature likely due to the softening of the weld nugget [39]. In contrast, welding through a previously stirred zone of a cast feedstock weld resulted in larger response variables than the initial weld pass of unprocessed cast 2050.

Intuitive, but observed from these builds and data is the effect of pin length on feedback forces from the process. The slower/thicker/cast build with exhibits much higher response forces and sampled temperature—which is logical as it had thicker material and a longer pin. Both faster/thinner builds resulted in similar feedback forces and temperature however with the previously discussed slight increase of response variables for T3 build.

The logged weld data revealed a total of 3.3 meters of weld to complete all layers of the thicker/slower/cast build. The thinner/faster cast build required 6.3 m, and the thinner T3 build ended with 6.4 m. Although the thicker cast build was performed with less total weld distance, the energy per unit length and total build energy greatly exceeded the thinner builds.

With the above considerations, the configuration with the lowest response variables is that of the thinner, faster cast build. These welds experienced lower temperatures and forces overall. As stated before, the thicker/cast layer build experienced the highest forces and temperatures. In-plane forces, torque and corresponding power in this case was almost double that of the two smaller builds. The all-T3 build was much closer in response variables to its cast counterpart but presented slightly higher temperatures and forces due to the bulk material choice.

3.2 Metallography

3.2.1 Macro Cross-Sectional Images

Samples from the weld builds were cut, processed, and analyzed with the procedures mentioned in the preceding chapter. Macro observations of the final polished and etched build cross sections can be seen in Figures 3.3 through 3.5. They highlight the geometric differences between the pins and lap plate thicknesses. It is also much easier to distinguish the overlapping double pass welds for the slower/thicker/cast build as compared to the two smaller builds that had a lesser value of this metric. Immediately noticeable is that all three builds are uniform in appearance and free of large defects.

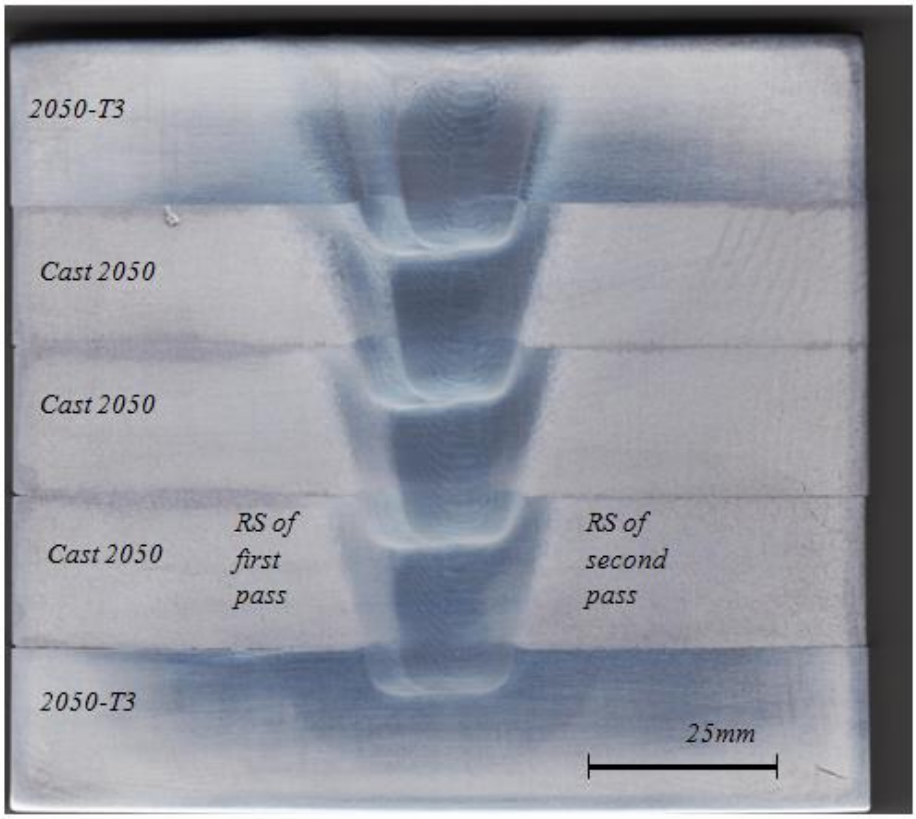

Figure 3.3 Slower/thicker/cast build cross section

Figure 3.4 Faster/thinner/cast build cross section

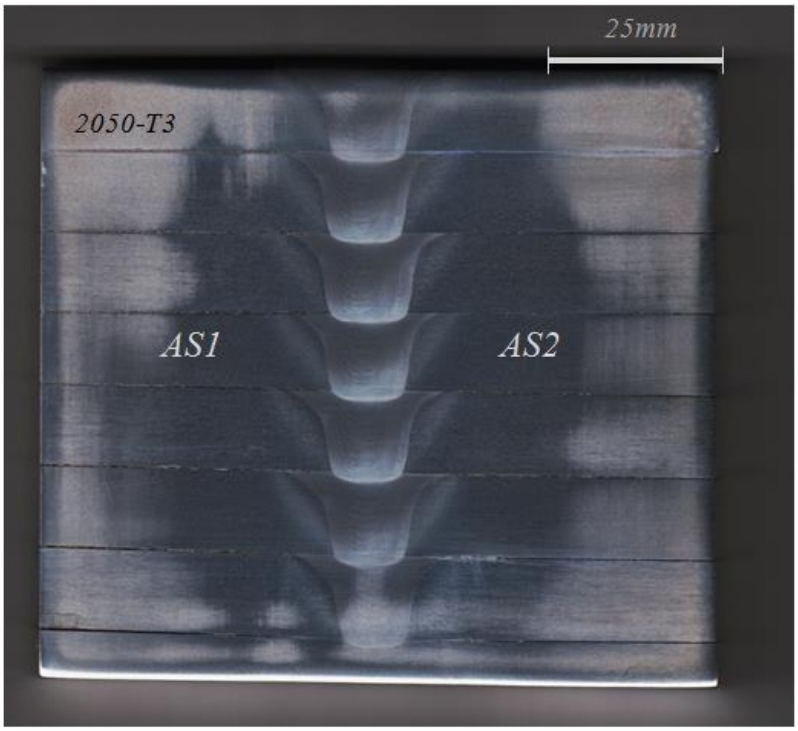

Figure 3.5 Faster/thinner/T3 build cross section

3.2.2 Usable nugget width

Extremely relevant to the additive manufacturing process is the amount of nugget free of the CLD. These regions would dictate the dimensions of the final additively manufactured component. Figure 3.6 of the thicker/slower/T3 build shows an estimated CLD-unaffected stir zone to be at 8 millimeters at the center of the build. However, it is noticeable that the amount of usable nugget is less than the total length of residual interface even after the double pass weld procedure. Some advancing side defects were also noticed in this specific build, as displayed in Figure 3.7. However, this was only noticed in close inspection of the top T3 layer, and not within the cast middle sections.

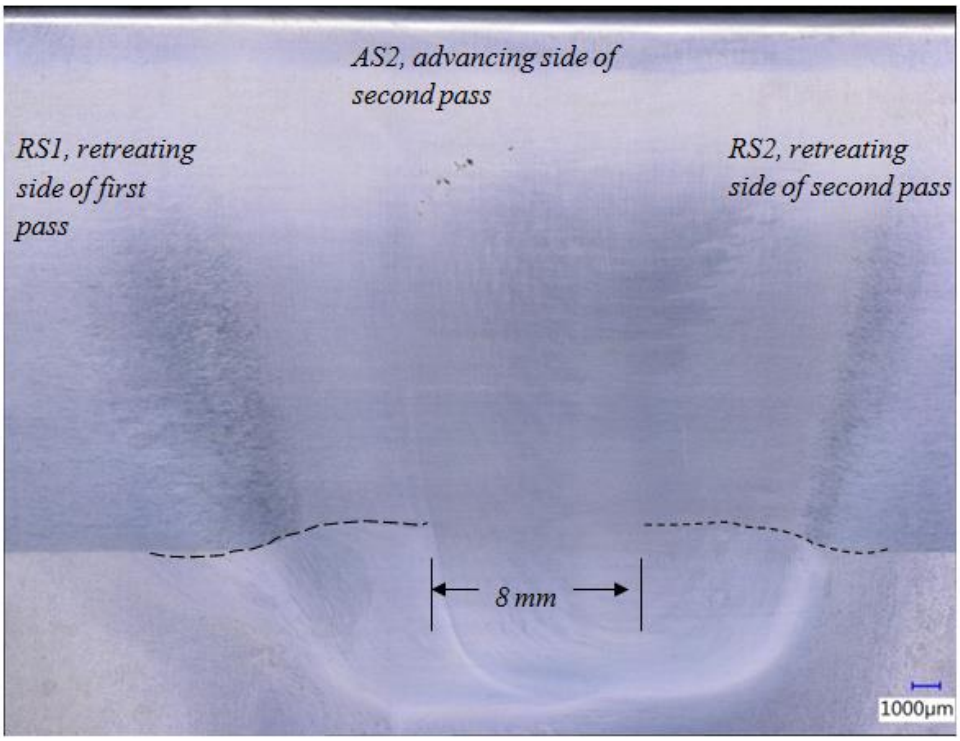

Figure 3.6 Usable nugget width measured in thicker/slower/cast build

Figure 3.7 Advancing side defects of the slower/thicker/cast build T3 top layer

The amount of unaffected weld material in between the double passes of the faster/thinner/cast build was estimated at over 7 millimeters using optical microscopy, shown in Figure 3.8 below. No consolidation-related defects were seen in this build and the interface appears quite disrupted within the mid-build cast layers, as presented in Figures 3.9 and 3.10.

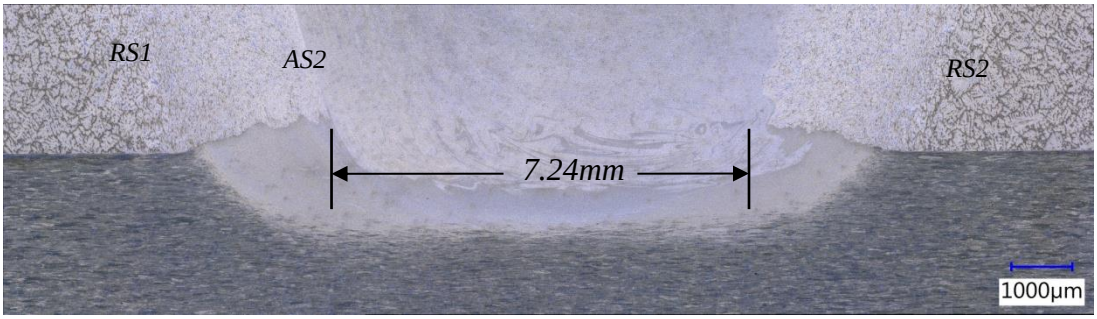

Figure 3.8 Thinner/faster/cast build usable weld nugget dimensions

Figure 3.9 Thinner/faster/cast build first retreating side (RS1)

Figure 3.10 Thinner/faster/cast build second retreating side (RS2)

As the geometry was similar for the cast and wrought small pin builds, the thinner/faster/T3 build was expected to remain very similar to that of its cast counterpart with regards to the cold lap defect and unaffected area. However, as previously mentioned in the Process section, after welding it was apparent that this build had been performed backwards—that is to say, the retreating sides of both passes instead of the advancing sides were captured in the stirred zone. Images of the two nugget sides are shown in Figures 3.11 and 3.12 which demonstrate the fortunate lack of visible CLD into the nugget area.

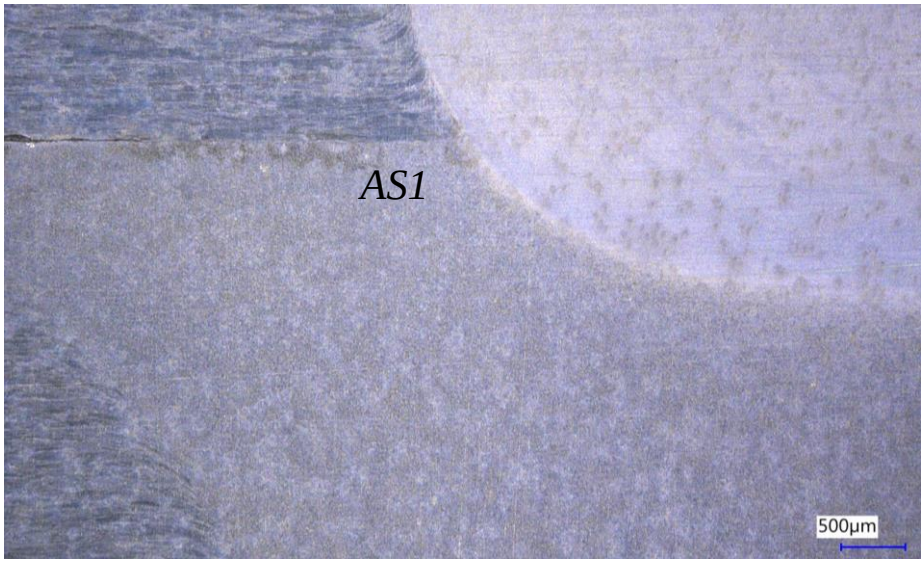

Figure 3.11 First advancing side of the thinner/faster/T3 build

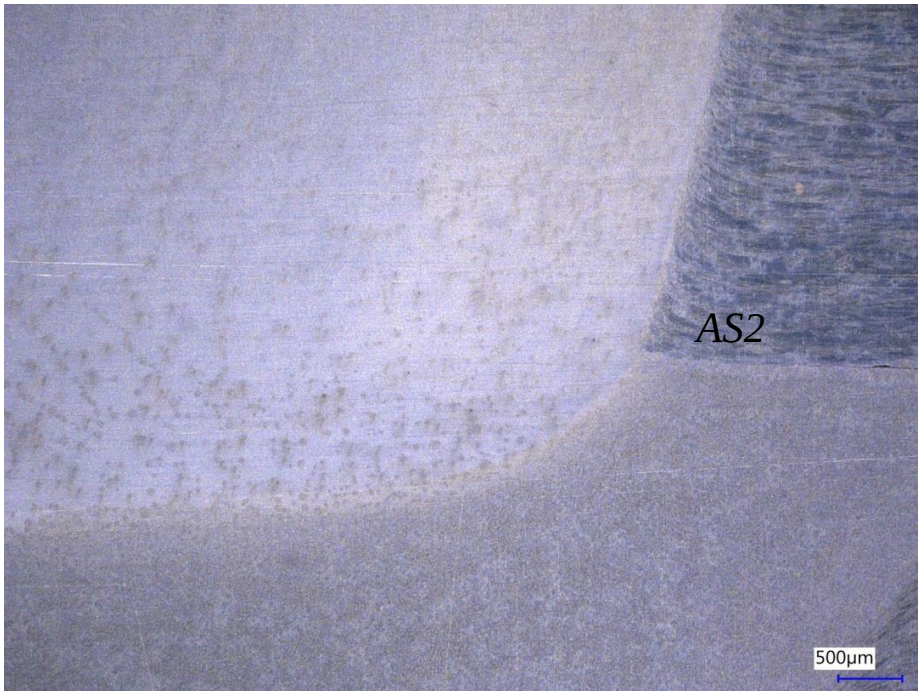

Figure 3.12 Second advancing side of the thinner/faster/T3 build

In general, from macrographic observations of both builds, the largest pin and lap width resulted in a large, visible interface CLD in the welded nugget but rendered a total usable amount of nugget of 8 mm thickness. The smaller builds exhibit no large defects, adequate visible disruption of the interface, and over 7.2 mm of usable nugget width in the case of the smaller cast build. In the case of the T3 build—which had been unintentionally performed with two advancing sides—there appeared to be no residual interface in the weld nugget.

3.3 Hardness

3.3.1 Horizontal Hardness Analysis

The hardness analysis was first performed at the pin midplanes of different locations within the cross sections as defined in the previous Process chapter. Demonstrated in Figure 3.13 on the next page, the processed cast mid-section of the thicker/slower/cast build exceeded the nugget strength of the 2050-T3 top layer in both as-welded and PWHT conditions. Unfortunately, this build did not have a midplane substrate plate hardness analysis to compare with the smaller builds.

Horizontal hardness was plotted in Figure 3.14 for the thinner/faster/T3 build at the pin midplanes of top, mid, and substrate layers. The initial observation of this analysis was that of the base T3 recovery in both the top and substrate layers. In fact, the applied aging treatment used in this study brings base T3 material up to the strength of 2050-T8, at approximately 190 HV. The welded material of the cast-mid layers showed some strength recovery with the heat treatment within this analysis, but not to the degree of the T3 layers.

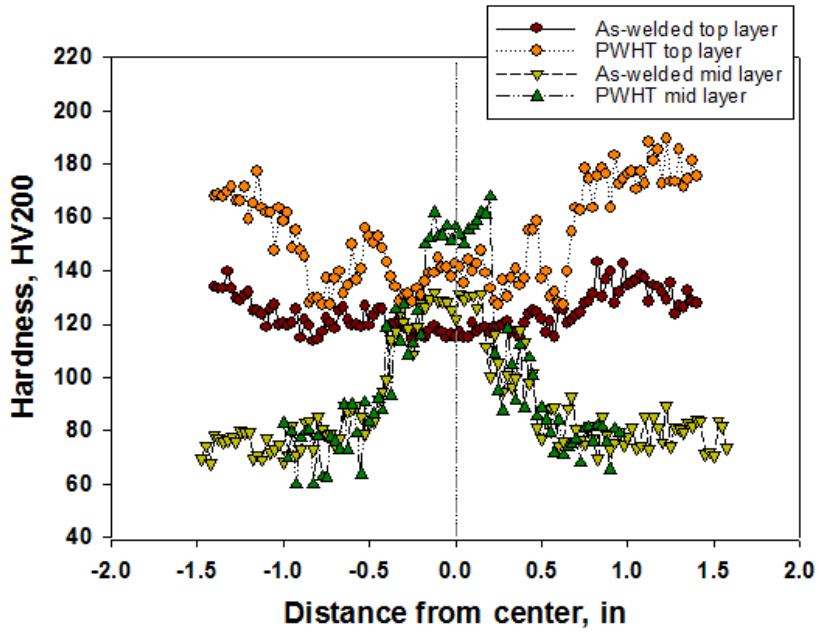

Figure 3.13 Midplane layer hardness of thicker/slower/cast build

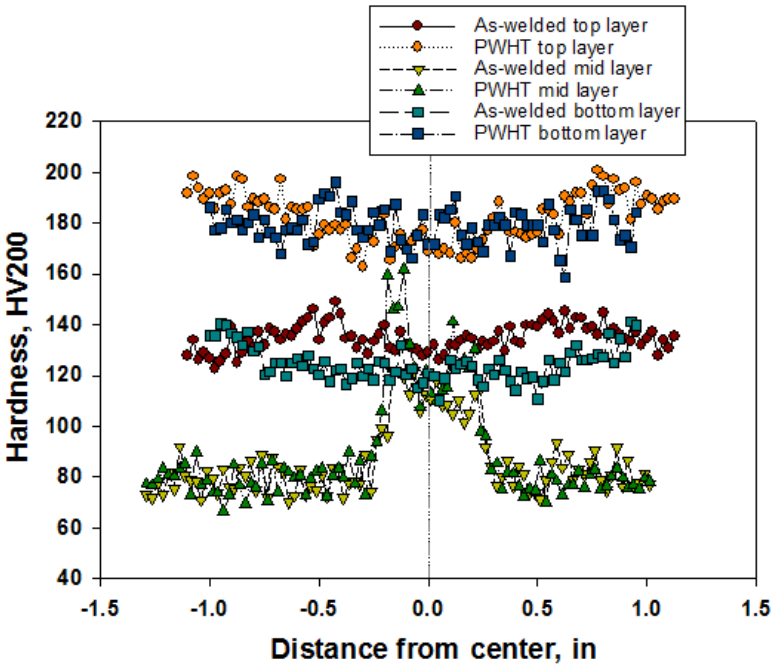

Figure 3.14 Midplane layer hardness of thinner/faster/cast build

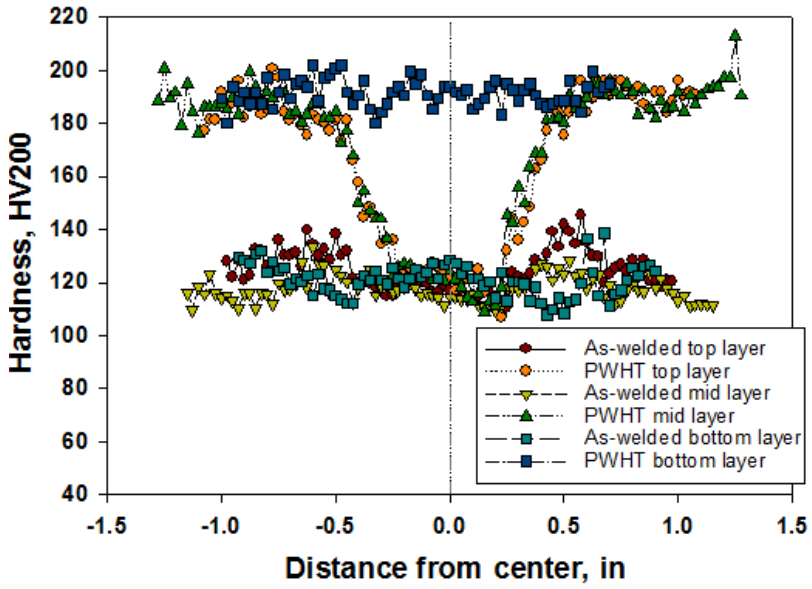

Figure 3.15 Midplane layer hardness of thinner/faster/T3 build

The all-T3 thinner/faster build horizontal hardness analysis is shown above in Figure 3.15. Initial observation indicates a recovery of the substrate hardness, however from this analysis the top and mid layers do not appear to increase in strength after aging. This is not thought to be true after observations with the previous builds, so this result will be explored further in the subsequent section.

The most important conclusion from horizontal hardness analysis for these builds is the observation of minimal variation in hardness occurring over the usable width of the weld nuggets. It is important to note that measurements at pin or layer midplanes are highly subjective to user choice, as they reflect a local property at a casually estimated location. Large variations with hardness are then possible when comparing between the builds and are not an accurate representation of hardness behavior throughout. Therefore, this is not the most precise analysis to gauge the properties of FSAM.

3.3.2 Vertical Hardness Analysis

In comparison to the horizontal hardness results, vertical microhardness hardness analysis for all three builds provides an analysis for hardness as a function of depth.

A vertical plot of the thicker/slower/cast build's hardness from the top layer through the z-direction depth is shown in Fig. 3.16. At first glance, the inhomogeneous distribution throughout depth is immediately noticeable. It can also be observed that the average hardness of each layer decreased slightly as the next layer was welded on top. The PWHT reversed this trend and resulted with a general tendency of increasing average nugget hardness through the depth until peak condition base metal was reached.

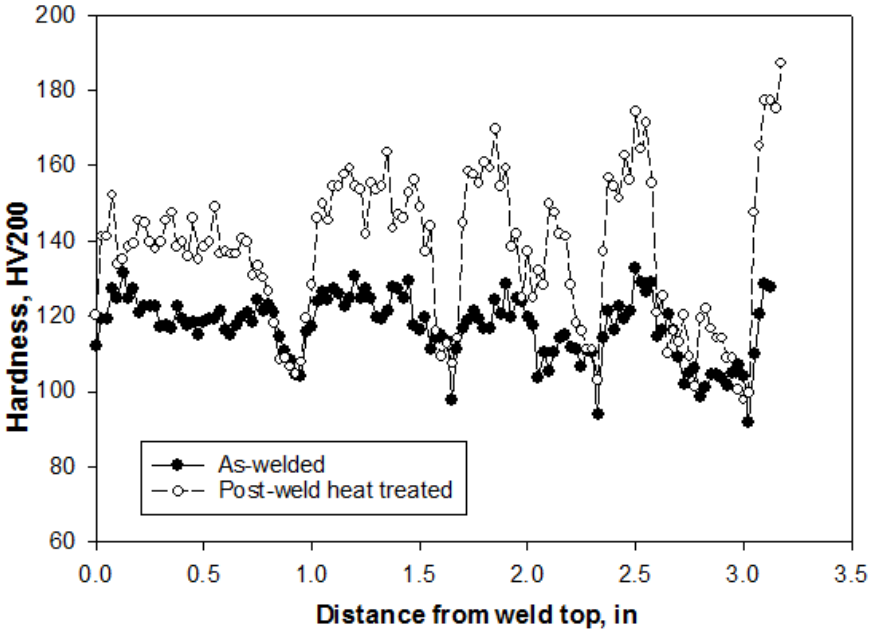

Figure 3.16 Thicker/slower/cast hardness through layers

Minimum hardness values within this build are shown to be at four different locations. This corresponds exactly with the number of lap weld layers that were used to fabricate the final build. More so, these areas show almost no recovered strength after the

heat treatment. Hardness data overlaid on the macro cross sectional image of Figure 3.17 show that these regions of interest are occurring at the base of each lap weld nugget, towards the bottom of the pin.

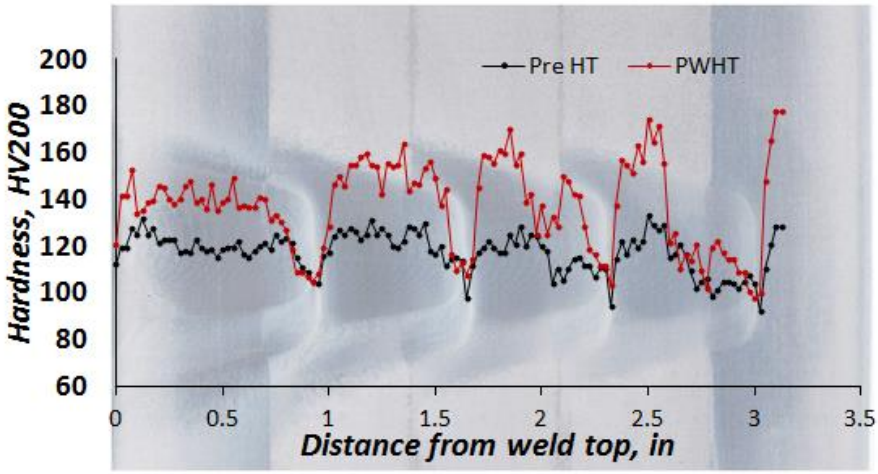

Figure 3.17 Thicker/slower/cast build hardness overlaid with cross section

Similar trends with the hardness distribution were also seen through-thickness with the thinner/faster/cast build as shown in Figure 3.18. In the case of this build, there were seven lap layers, and these are shown in the corresponding individual areas of minimum hardness. Again, the lack of strength recovery in some areas was visible. It appears that the proportion of recovered nugget is much less than that of its thicker build counterpart, but the maximums experienced were higher. A visual of hardness and locations through the build are shown in Figure 3.19. Like the thicker cast build, minimums are once again at the transition zone (TZ) in between lap weld layers. Mid-build layers demonstrated substantial strength only in the top of each layer which rapidly decreased towards the bottom of the lap weld nuggets.

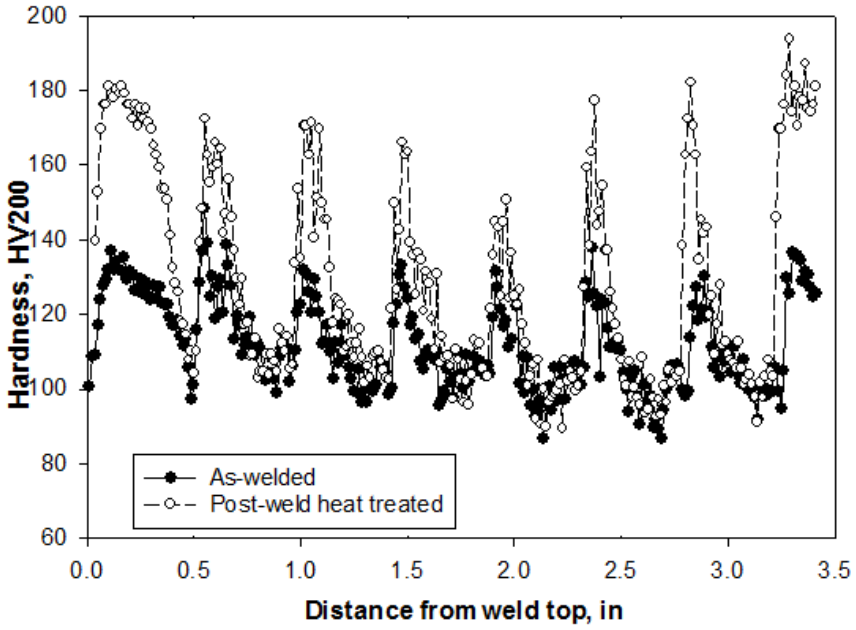

Figure 3.18 Thinner/faster/cast build hardness through layers

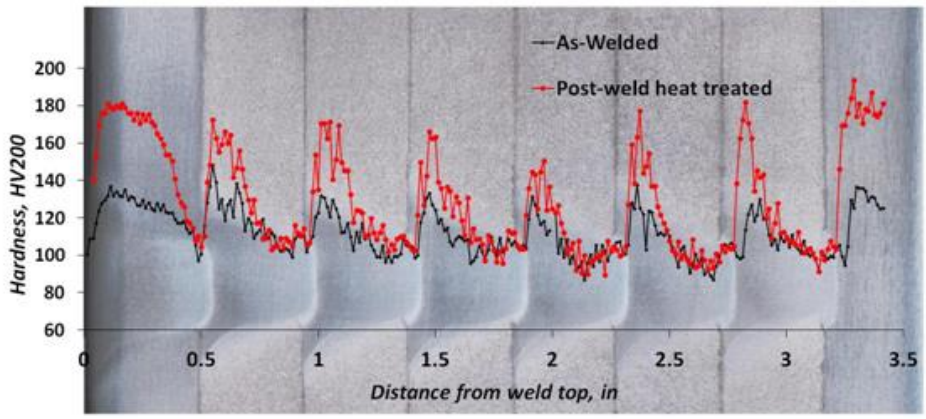

Figure 3.19 Thinner/faster/cast build hardness overlaid with cross section

Recall that the hardness analysis of the thinner/faster/T3 build from the horizontal interpretation in Figure 3.15 showed that the welded nugget recovered very little if at all within the midplane. The vertical microhardness analysis in Fig. 3.20 shows that this is not true as there is a substantial recovery mostly towards the upper pin areas of each welded layer. As has been seen in all the investigated builds, almost no recovery occurs at the areas

located towards the bottom of the pin length and within the transition zone in between lap layers. This is verified through examination of Figure 3.21 which again displays the lowest values corresponding to the areas of weld nugget associated with the bottom of the pins or the overlapping zones. When compared with the previous cast build with identical lap weld thickness and similar response variables, the hardness of this T3 build has both lower maximum and minimum values. However, unlike the cast build, nugget hardness is much more uniform in distribution.

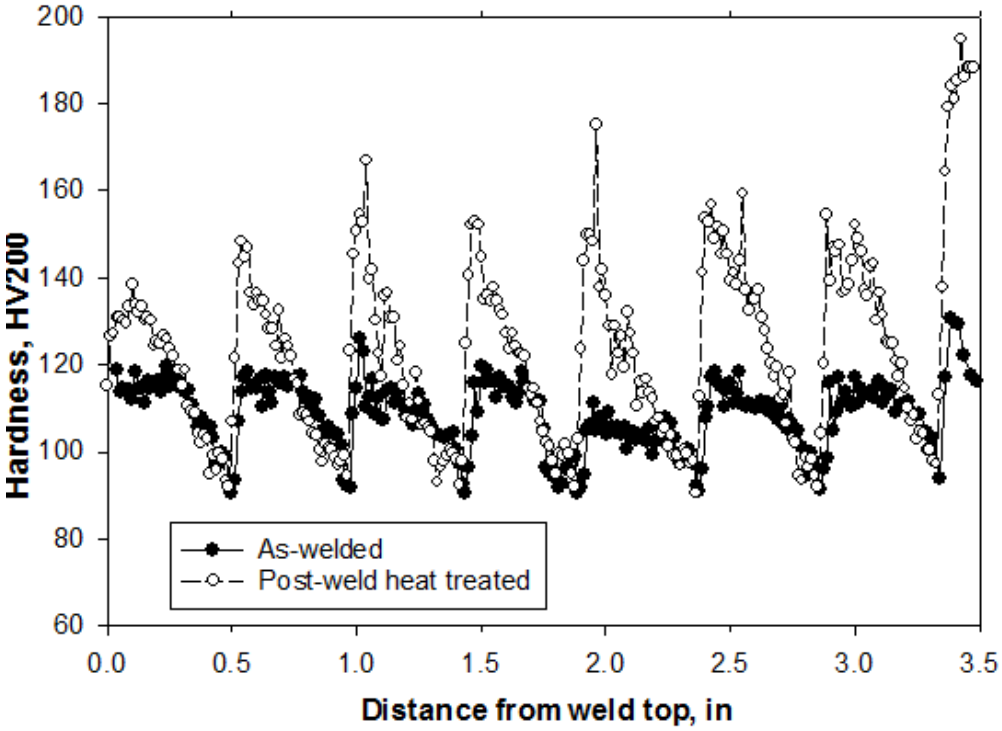

Figure 3.20 Through-thickness Vickers microhardness of the T3 build

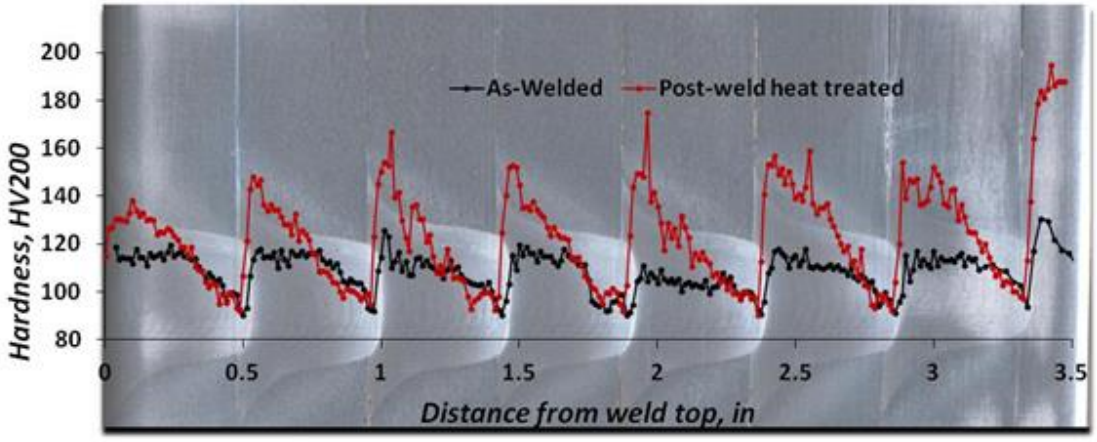

Figure 3.21 Thinner/faster/T3 build hardness overlaid with cross section

3.3.2 General Remarks

For all builds, average hardness of the welds in the as-welded state was shown to very slightly decrease as the distance away from the top layer increases. By performing a weld on the top surface of previous welded layers, the preceding plates were subject thermal cycles in different quantities depending on the number of layers added to the structure. This could possibly contribute to an annealing of the welds below, leading to coarsening of the precipitates and a reduction in hardness as seen in some of the as-welded build conditions. The hardness was also observed to be at minimums in the overlapping locations or transition zones (TZ) in between layers for all builds. This is consistent with previous studies of lap welding additive manufacturing—and attributed to the thermal conditions associated with the process [14-15].

All builds displayed inhomogeneous behavior throughout the layers with high and low hardness values dependent on location. The lowest hardness values corresponded closely with TZ between layers which includes areas towards the bottommost tip of the welding

tool and possibly the adjacent HAZ created through this process. The smaller build from cast material showed both increased minimum hardness and larger maximum values after heat treatment as compared to the T3 build of similar lap geometry. However, the T3 build demonstrated a more uniform recovery across the nugget compared to its cast counterpart. Of all the builds, however, the thicker cast build demonstrated the highest proportions of uniformity and recovery, indicating that more of the weld nugget for this build was held above the solution heat treating temperature.

3.4 Tensile Testing

3.4.1 Stress-Strain Results For All Builds

Uniaxial tension tests were performed using the procedures outlined in Chapter 2. Figure 3.22 on the next page displays the engineering stress and average strain curve results for the thicker/slower/cast build. Ultimate tensile strength in the as-welded condition reached up to 382 MPa, however for the PWHT samples, this value only reached an average of 352 MPa. Maximum elongation for the conditions were reported as 8.3 and 6.9 % for the as-welded and PWHT conditions respectively. From this build analysis, samples with the aging treatment showed a reduction in both ultimate tensile strength and elongation. Behavior within the elastic regime is shown to be very uniform in any condition for this build.

The second build of cast material performed with thinner layers and a faster welding speed resulted in the data seen in Figure 3.23 on the next pages. Both tested PWHT samples have good uniformity and the elastic portions of all condition samples are consistent with those found in the previous build. In the as-welded and post-weld heat treated conditions,

the samples from this configuration show improved elongation as compared to the thicker build with maximums of 12.4 and 10.2% for the respective conditions. The ultimate strength of this build resulted in a reduction from 341 MPa in the as welded condition to that of 332 MPa with the aging treatment. This is a similar trend to that found in the thicker cast build samples, however the ultimate strength for this build is notably less than that of the previous thicker cast build results.

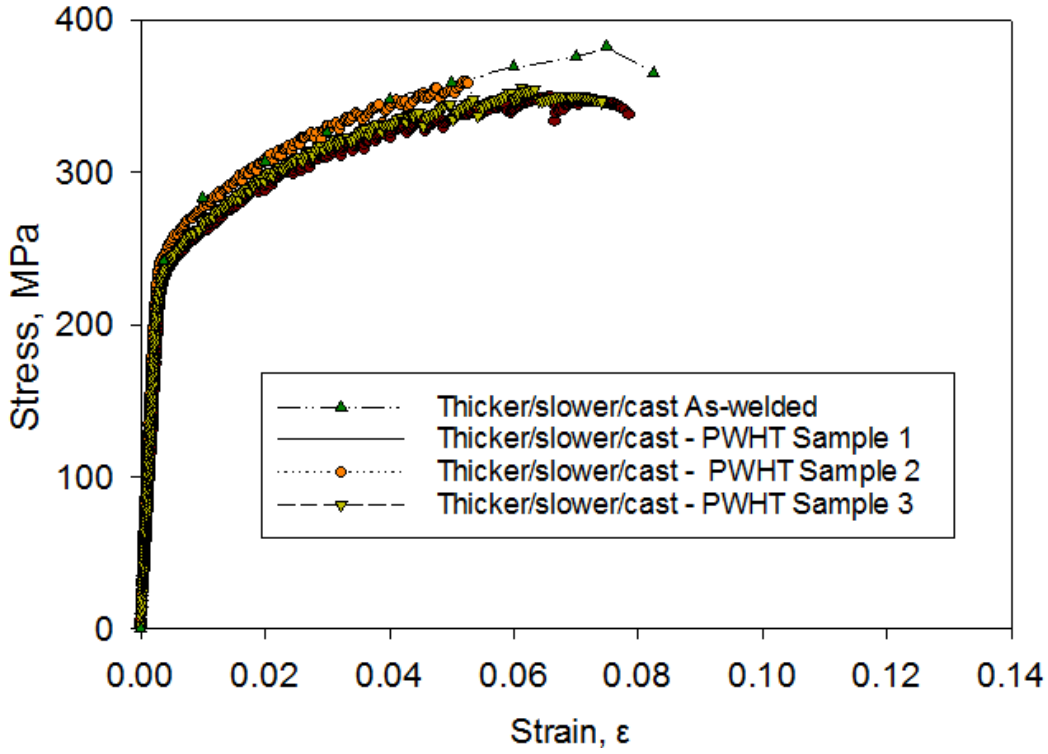

Figure 3.22 Engineering stress and average strain of thicker/slower/cast build

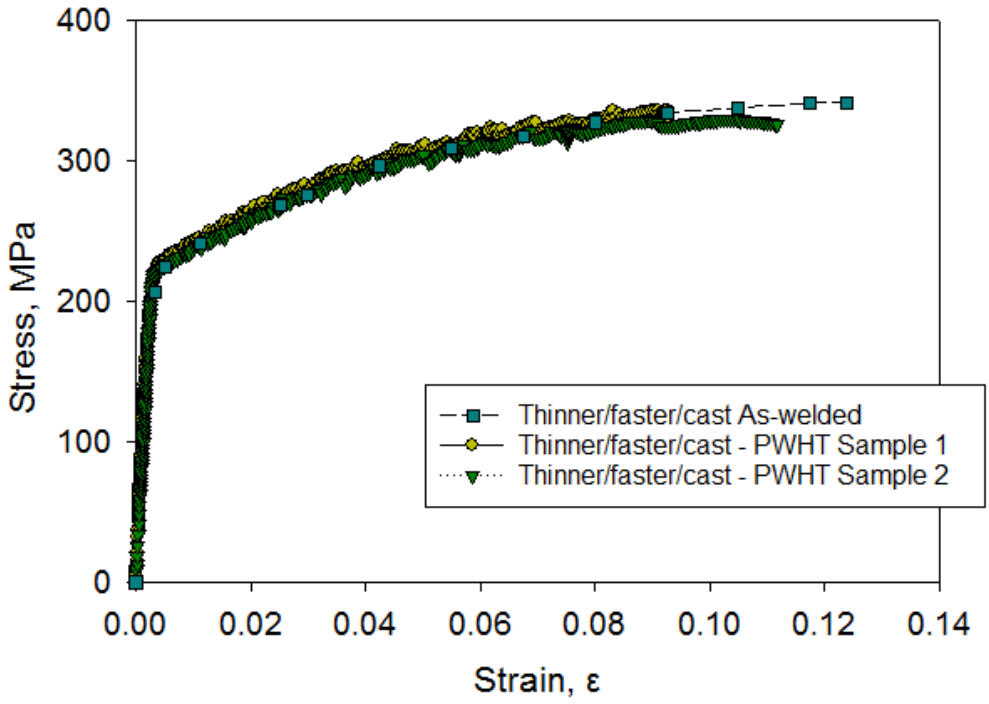

Figure 3.23 Engineering stress and average strain of thinner/faster/cast build

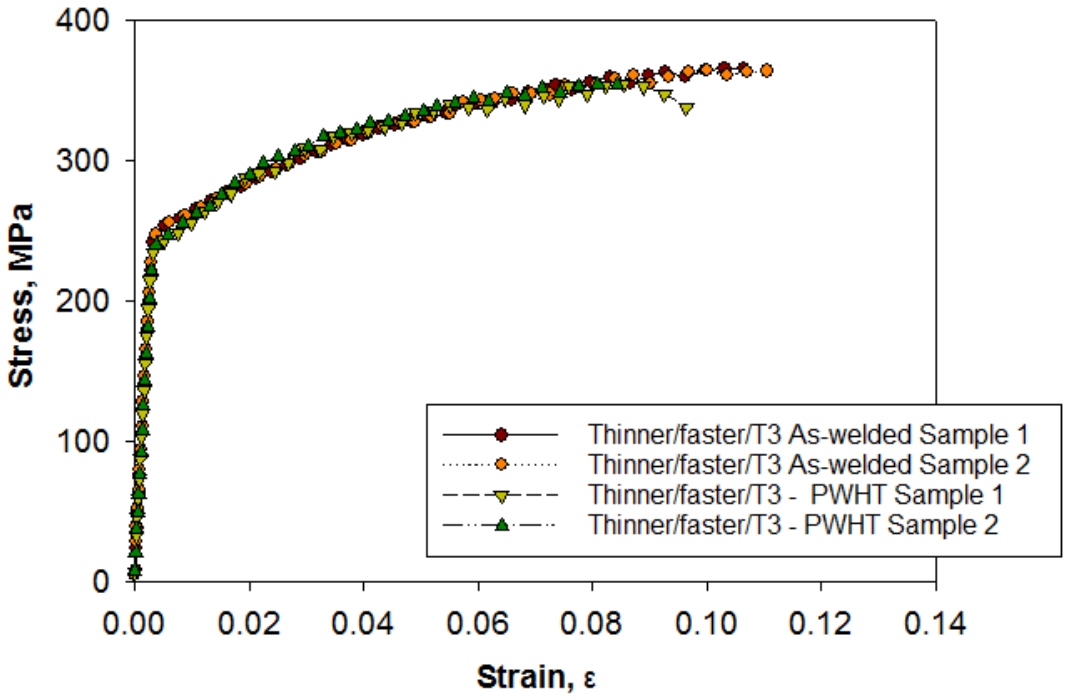

Figure 3.24 Engineering stress and average strain of thinner/faster/T3 build

In comparison to the two cast builds, stress-strain results from the T3 build that was performed with thinner and faster lap welds are shown in Figure 3.24 on the previous page. The as-welded condition resulted in an ultimate tensile strength of 365 MPa with a 10.9% average elongation in these samples. The aging treatment showed a decrease in these properties to a strength of 354 MPa and elongation of 9.1% which establishes a noticeable trend for all three FSAM builds investigated within this study.

3.4.2 Build Tensile Comparisons

Concise comparison charts are shown in Figures 3.25 and 3.26 below and on the next page for ultimate tensile strength and average elongations of all three builds. The only specimen that met and slightly exceeded cast 2050 base metal tensile strength was that of the as-welded thicker/slower cast build. None of the samples met the other feedstock material UTS of 2050-T3 (453 MPa) or approached that of monolithic T8 temper (540 MPa). As previously described, there was a noticeable trend of decrease in these mechanical properties reported after the post-weld heat treatment.

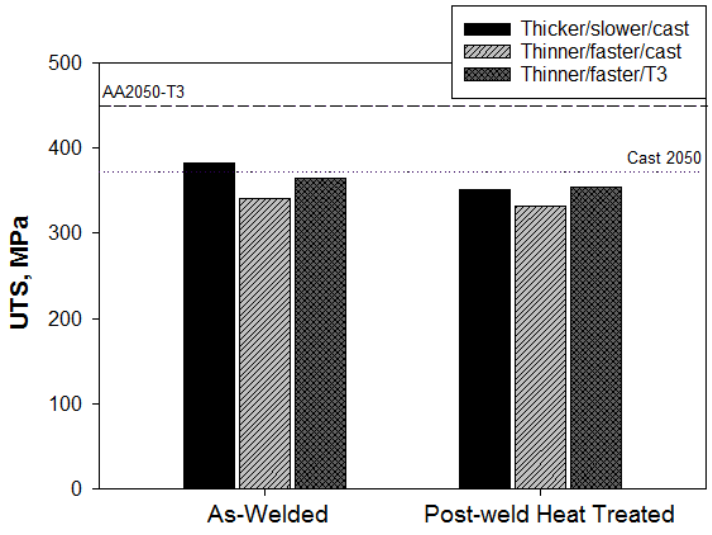

Figure 3.25 Comparison of FSAM builds ultimate tensile strength

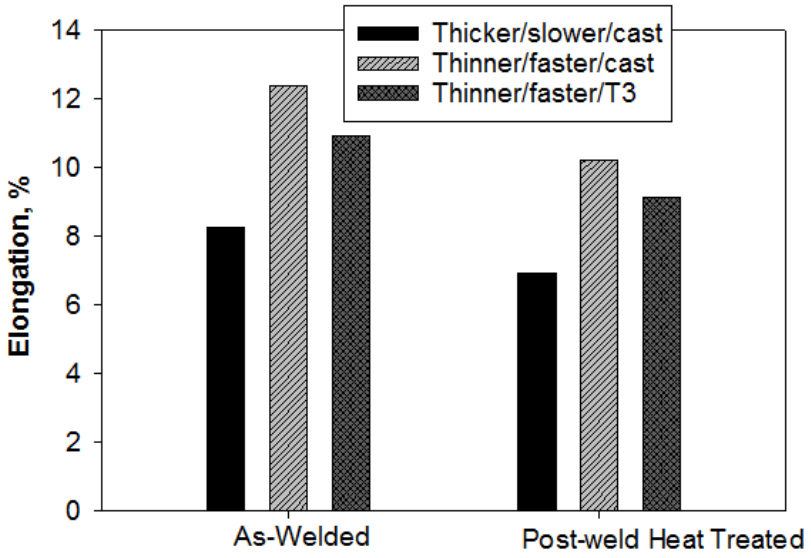

Figure 3.26 Comparison of average elongation in FSAM builds

Of the three configurations, the highest tensile strength in both conditions was shown be that of the thicker/slower cast build which resulted in an UTS efficiency in the as-welded state of up to 87% of 2050-T3. However, the highest elongations were reported with the thinner/faster cast build. The FSAM build made from T3 material resulted in intermediate properties of tensile strength and elongation compared to the two cast builds.

Figure 3.27 displays the engineering stress-strain curves of aged build samples with those of 2050-T3, 2050-T8 and cast 2050. As previously discussed, performance of the FSAM samples in the aged condition resulted in a lower UTS than the as-welded samples or base materials within this family—and in all cases a decrease in elongation.

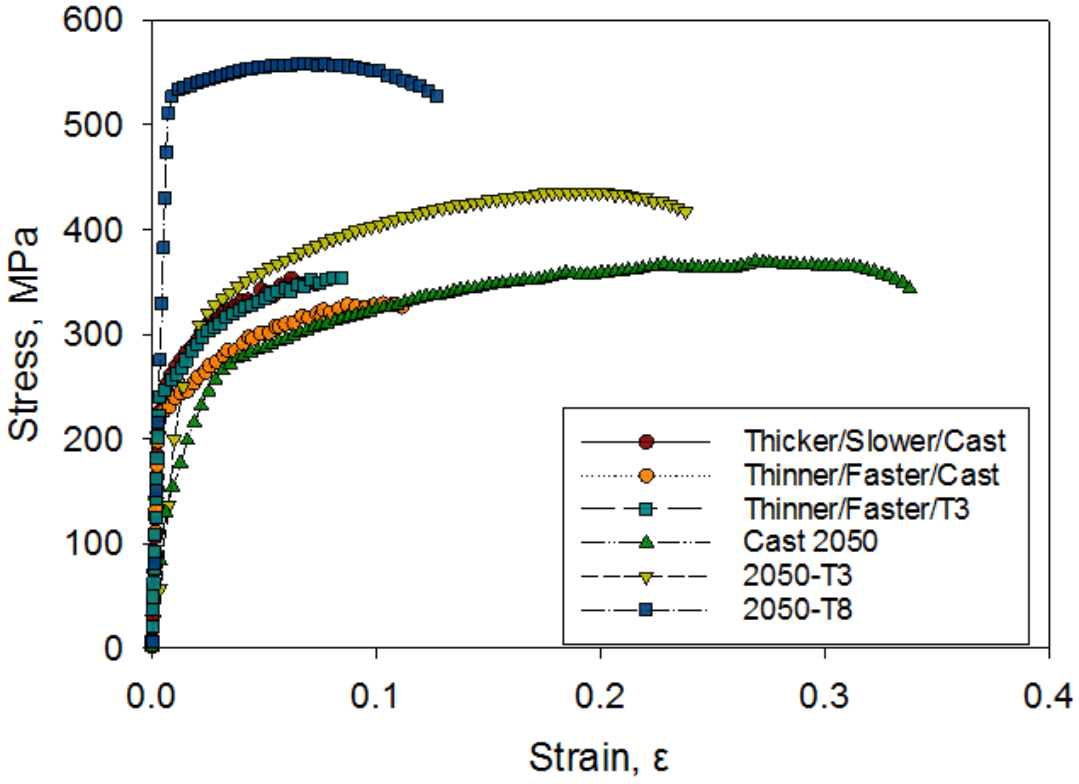

Figure 3.27 Stress-strain curves for FSAM builds and base materials

It is however important to note that the strain from the builds is an overall value indicating the performance of these samples, determined by an extensometer function of the digital image correlation software. Therefore, local measurements were not taken into consideration and any heterogeneity in mechanical properties would not be immediately obvious. This will be explored within the following subsections.

3.4.3 Strain Concentrations And Digital Image Correlation

Digital image correlation was used to identify the strain concentrations experienced in the FSAM samples under uniaxial tension. Displayed in Figure 3.28 with a 2050-T3 sample, these images were not captured at the time of failure, but at earlier moments to visibly see the patterns of strain.

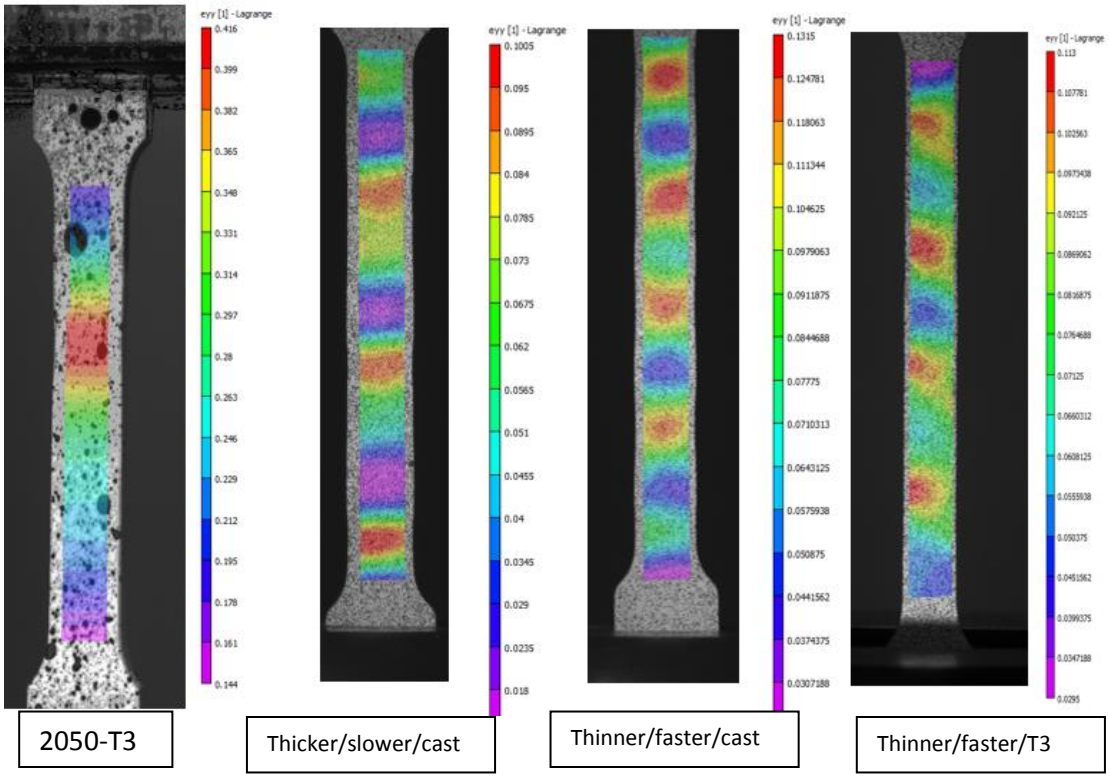

Figure 3.28 Strain concentrations calculated with DIC

As compared to base metal that tends to only concentrate strain at the single location of failure, the additively manufactured builds feature multiple high strain zones which correspond to the location of softened material in between layers—these are the same areas of the cross section that exhibited low hardness measurements with the previous section hardness analysis. Ultimately, the FSAM samples fracture at any one of these locations—examples of these are shown in Figure 3.29. The low average elongation and

ultimate tensile strength of these welded specimens as whole are a result of the softened areas in the welded builds where strain tends to concentrate [2].

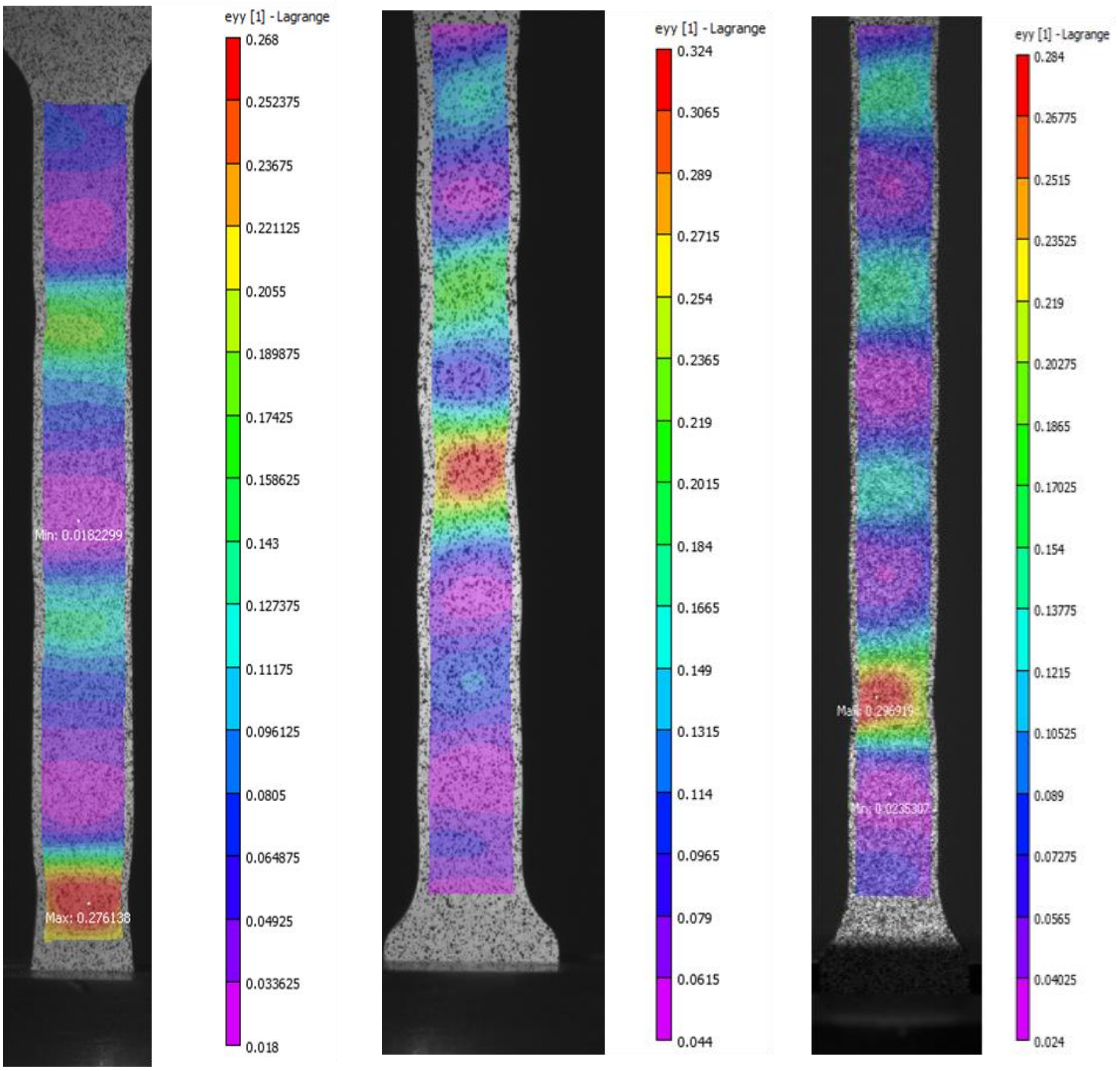

Thicker/slower/cast build with PWHT Thinner/faster/T3 build with PWHT Thinner/faster/cast build with PWHT

Fig. 3.29 Strain distributions at failure

The minimum and maximums of local strain at fracture are noted in Table 3.1 for all the builds and T3 temper samples. The FSAM builds show relatively similar values for the maximum strain concentrated at the point of failure. Welded samples showed local strain of 25-34% at failure and base metal in the T3 temper was almost to 53%. Lower values compared to T3 were also registered for the minimum local strains in the weld samples. Concisely, the local minimum or maximum strain values associated with the welded samples were less than those found in 2050-T3 in addition to observing multiple high strain areas within the tested builds.

Table 3.1 Strain concentrations at failure

Build	Minimum strain, ε	Maximum strain, ε
Slower/thicker/cast *PWHT*	0.015	0.275
Faster/thinner/cast *PWHT*	0.032	0.342
Faster/thinner/T3 *As-welded*	0.034	0.25
Faster/thinner/T3 *PWHT*	0.024	0.343
2050-T3	**0.2**	**0.516**

3.4.4 Fracture Surfaces Of T3 Build Tensile Samples

It was observed that the T3 build tensile samples contained prominent onion ring tool marks on their fracture surfaces, displayed in Figure 3.30. This is presented next to a

sample from the similarly lapped cast build for comparison purposes. The presence of this visible feature towards the base of the pin suggests that this build was performed with inadequate penetration and required more plunging force during the welding process [40].

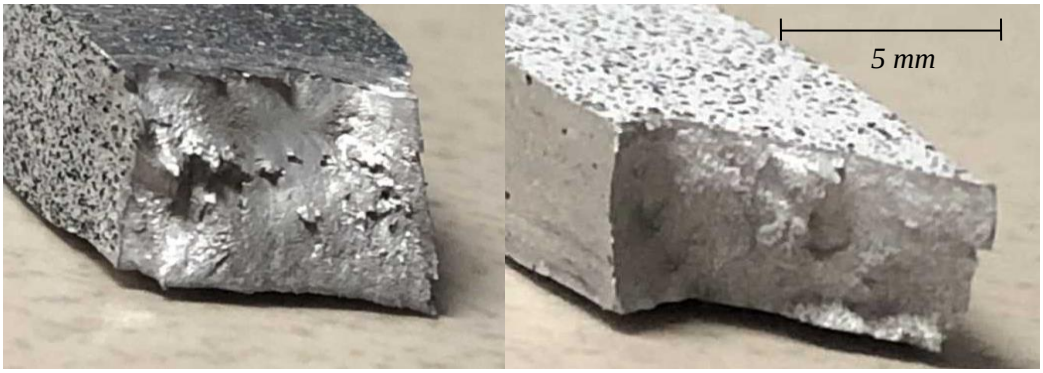

Thinner/faster/T3 with PWHT *Thinner/faster/cast with PWHT*

Fig. 3.30 Tool marks visible on T3 tensile fracture

3.4.5 General tensile analysis observations

As explored in the previous sections, engineering stress and average strains were explored for all welded builds and found to be in most cases below the ranges of 2050 cast, T3, and T8 temper base metals no matter the condition of the welded samples (as-welded or aged). The friction stir additive manufacturing process resulted in inhomogeneous strain distribution within the investigated builds during tensile uniaxial load. Areas of concentrated high strain corresponded to the same locations of minimum hardness and were always the sites of failure in tensile tests.

3.5 Fracture Testing

3.5.1 K-Δa Curve Results

Using the methods described in Chapter 2, a fracture analysis was performed for the FSAM process builds. Stress intensity plotted against crack growth is shown in Figure 3.31 which includes all aged FSAM build samples and that of monolithic T8 taken from the short-transverse (S-T) rolling direction. The calculated fracture toughness of base metal corresponded well to that found in literature [41]. An initial observation of this plot shows most of the welded samples displayed higher stress intensity than the base metal values, though demonstrated similar overall crack growth.

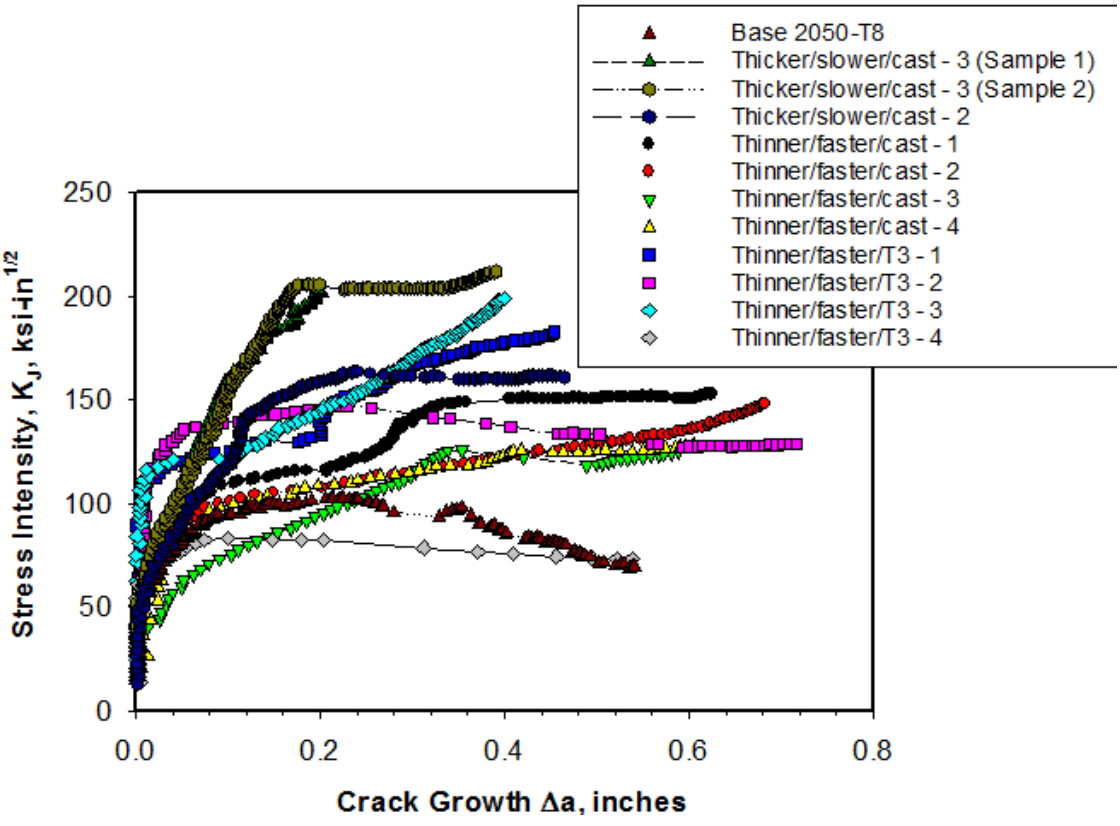

Fig. 3.31 K_J-Δa curves of fracture analysis

Of the builds, the thicker/slower/cast build exhibited the highest observed fracture resistance with the samples which grew cracks through the welded layers. The two thinner builds of cast and T3 had reasonably similar appearances overall, but the lowest experienced value of fracture resistance was seen by the thinner/faster/T3 build in orientation -2 which corresponds to crack growth parallel to the welding direction.

Some samples are observed to exhibit curves with sudden increases in resistance. Most of these correspond to the odd-numbered orientations of -1 and -3 which are given to crack growth through weld thickness layers. Noticeably, many of the even-numbered samples of -2 and -4 show stable curves with gradual increase in resistance. These samples correspond to crack growth parallel to the welding direction at approximate midplane of the builds. The overall fracture behavior can be explained through the interaction of strong/weak interfaces—growth parallel to the welding direction follows along weaker interfaces which appear as stable, predictable curves. In contrast, when fracture is initiated through the welded layers, the strong/weak interfaces demonstrate crack stopper behavior similar to that of a composite material and sudden changes in resistance are seen. Most importantly, this indicates that crack growth orientation with respect to weld direction had a large effect on the behavior of the additively manufactured samples.

3.5.2 Fracture Surfaces

The monolithic AA2050-T8 samples displayed very predictable and stable fracture along the same plane as the initial pre-crack, shown in the figure on the next page. The

surfaces were uniform in appearance which corresponded with the generally steady R-curve results.

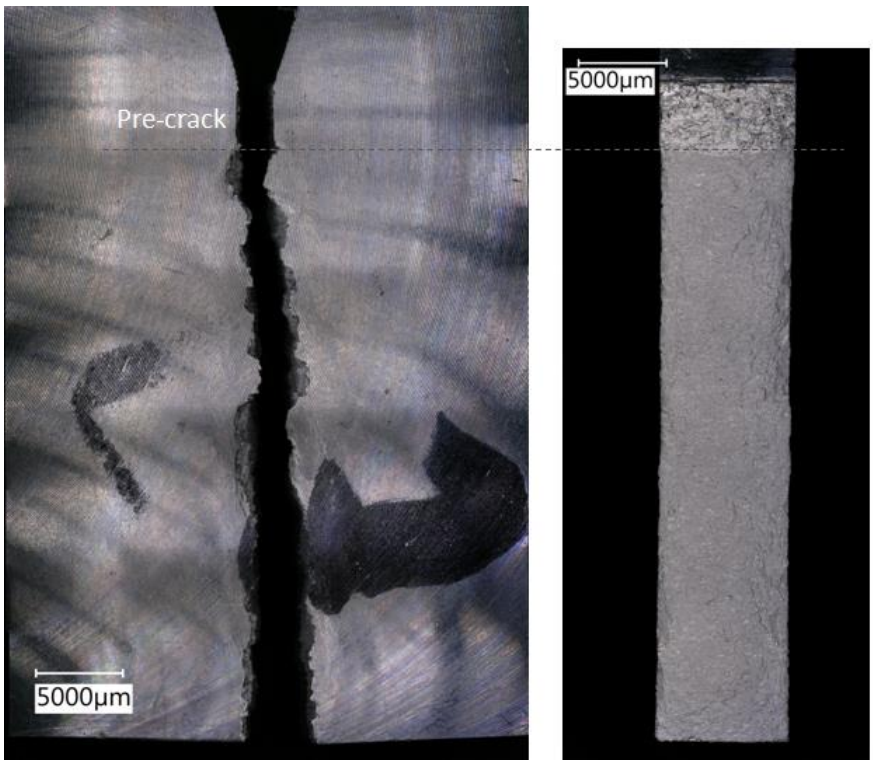

Fig. 3.32 Fracture surfaces of 2050-T8 base material

The specimens from the thicker/slower/cast build displayed jagged fracture surfaces with no definite trends as far as the direction of crack propagation with respect to welding direction. However, the polished sides shown in Figure 3.33 demonstrate that changes in mode, behavior, or fracture resistance could likely be attributed to the cracks seeking weak areas in the weld builds. Shown by the hardness distributions through the layers and tensile test stress concentrations, there are strong/weak interfaces present in the investigated FSAM builds as a result of the process.

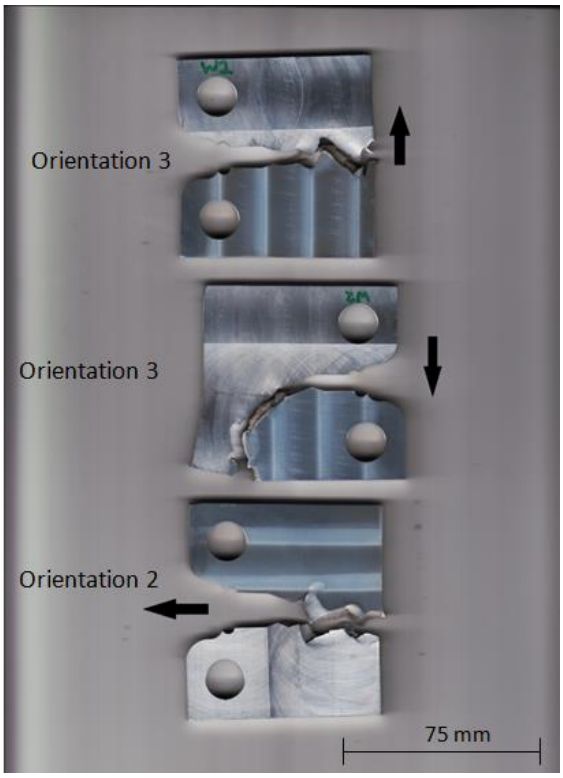

Fig. 3.33 Fracture appearances of the thicker/slower/cast build samples

Build samples from the thinner/faster/cast FSAM configuration exhibited fractures that wandered in direction from the nominal crack plane and included some very mild onion ring marks at the locations of pre-crack. These are shown in Figures 3.34 and 3.35 on the next page. The jagged appearing samples of orientations -1 and -3 showed some distinctive artifacts within the fracture structure at several locations corresponding with lap weld transition zones. This reinforces the explanation for sudden changes in fracture resistance related to these sample orientations. The sample orientations -2 and -4 which denoted crack orientation parallel to the weld travel did not show the same interface defects and were also the orientations that displayed smoother R-curves.

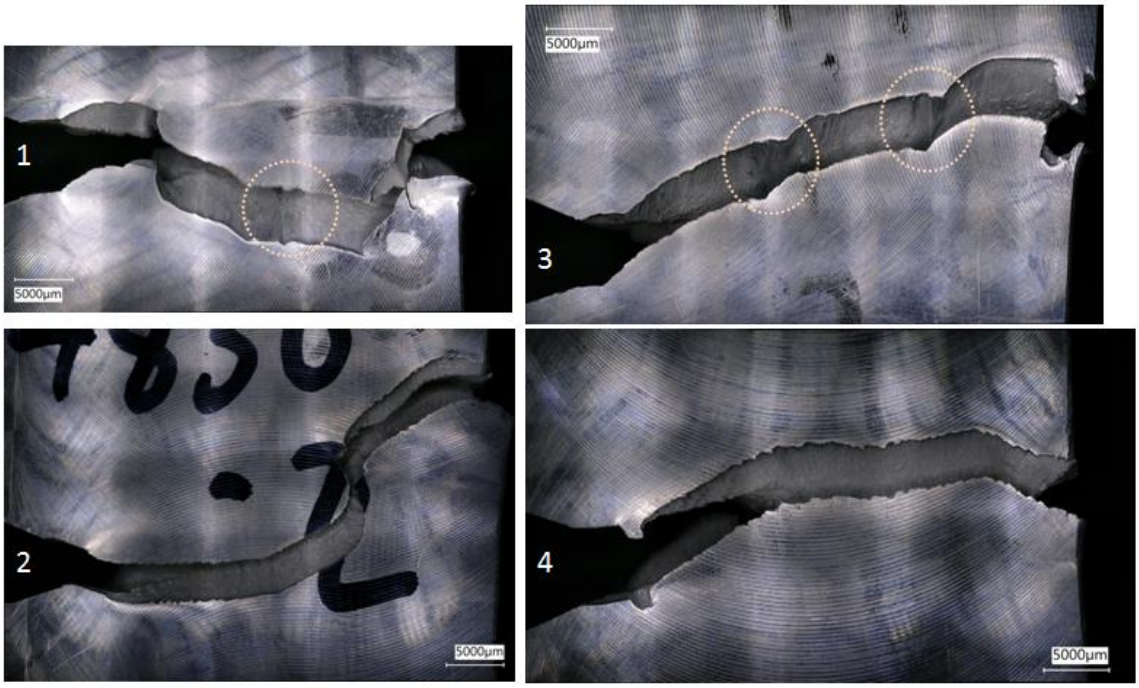

Fig. 3.34 Fracture surfaces from the side view for thinner/faster/cast build samples

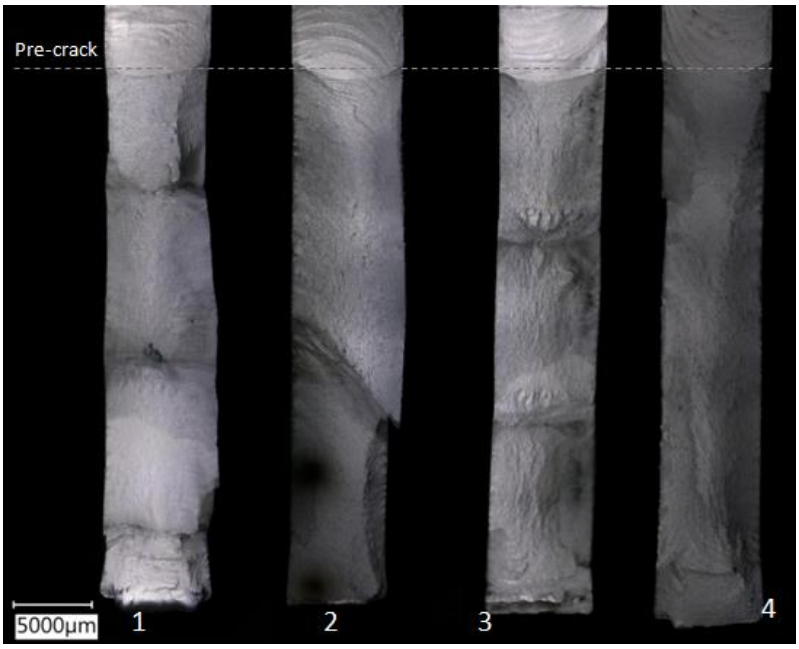

Fig. 3.35 Inner fracture surfaces of thinner/faster/cast build

Samples that grew cracks through weld layers of the faster/thinner/T3 feedstock build (orientations -1 and -3) did not as-prominently exhibit layer artifacts compared to the welded build but did display very jagged fractures and slight layer artifacts. Importantly, it was observed that samples from this build with crack growth orientation parallel to weld travel exhibited extremely pronounced onion ring tool marks, similar to those seen in the tensile test samples. This is shown in the figures 3.36 and 3.37 below and on the next page and emphasizes the severity of the lack of plunge force with this build. It appears that from the nominal pre-crack plane, the fracture itself jumped to a close, under-plunged plane of weakness and continued the propagation along this plane. The general fracture resistance of these samples was still high regardless of the process fault.

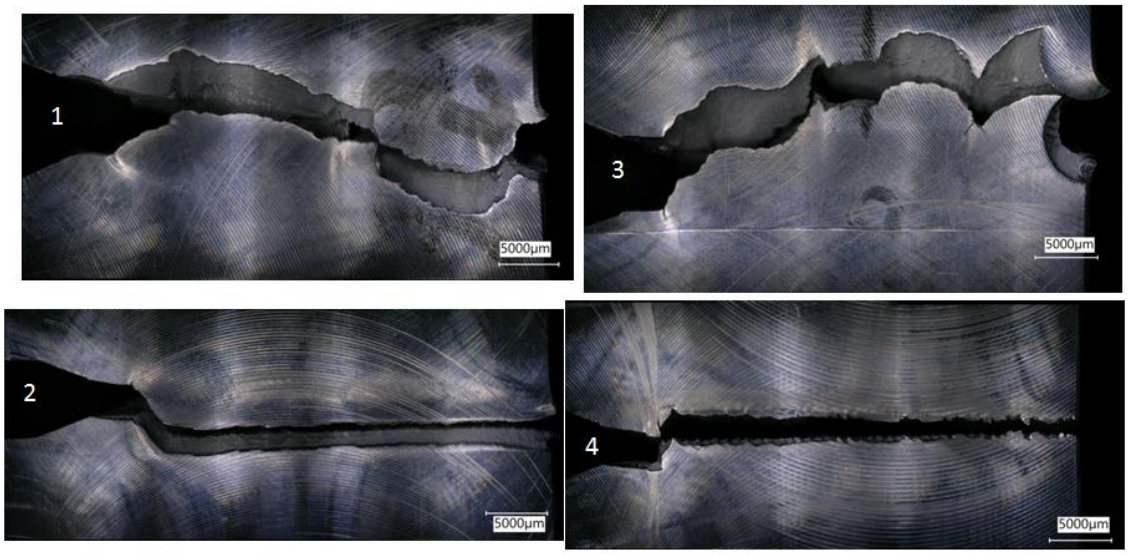

Fig. 3.36 Fracture appearance of thinner/faster/T3 build from side view

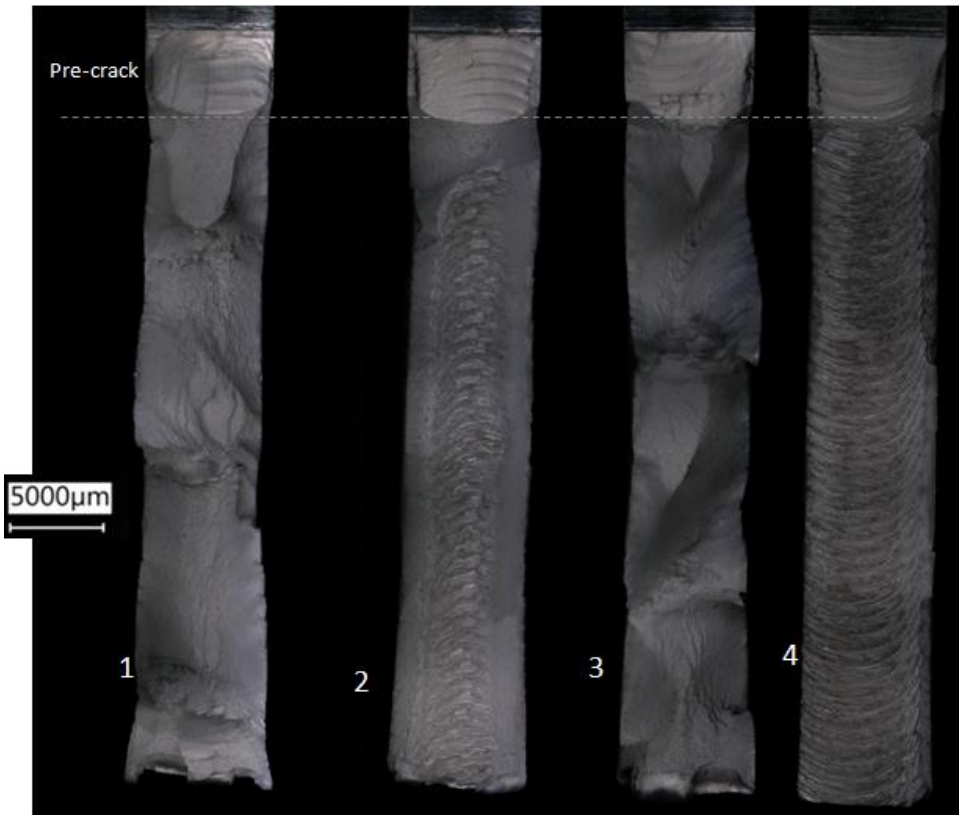

Fig. 3.37 Inner face fracture surfaces of the thinner/faster/T3 FSAM build

3.6 Summary Of Results

3.6.1 Weld Process

- Overall temperature and response forces were the highest in the thicker/slower/cast build.
- Though the thicker cast build had shorter total weld length compared to the thinner builds, it still contained the total highest build energy
- The responses for the two thinner builds were similar, however the T3 build showed slightly greater values.

3.6.2 Metallography Analysis

- All build cross sections appeared uniform and free of major defects
- The thicker/slower/cast build resulted in a cold lap defect-free useable nugget width of 8 mm
- A CLD-free usable nugget width of 7.2 mm was established for the thinner/faster cast build
- The thinner/faster/T3 build was found to have been manufactured incorrectly but no CLD was observed in this build using macrographic methods

3.6.3 Hardness Analysis

- All builds presented inhomogeneous hardness distributions
- Much of the PWHT nugget when examined through lap layers exceeded cast and T3 base strength—However, areas of low hardness were found distributed through the build depth

- These reported minimum values were located at the transition zones in between lap weld layers. These areas also did not recover strength with the post-weld heat treatment
- The thicker/slower cast build displayed the most consistent hardness distribution in both as-welded and with a PWHT. This is likely due to more of the nugget held above the solution heat treating temperature during the welding process

3.6.4 Tensile Analysis

- Builds exhibited multiple strain concentrations throughout the tensile samples
    - Located at the weaker minimum-hardness transition zones
- Largely, tensile performance was less than that of base cast 2050, 2050-T3, and 2050-T8 with both ultimate tensile strength and average elongation
- Of the three builds, the highest UTS was achieved in the as-welded thicker/slower/cast build. Largest average elongation was observed in the thinner/faster/cast build in as-welded condition
- Process underplunge tool marks were observed on the tensile fracture surfaces of the T3 build samples

3.6.5 Fracture Analysis

- In general, fracture resistance of welded samples was higher than that of monolithic 2050-T8

- The slower/thicker/cast build demonstrated the highest fracture resistance of the FSAM builds and both thinner builds showed similar fracture resistance and crack growth
- Fracture behavior of these FSAM builds showed dependence of crack growth orientation with respect to welding direction—interaction of strong/weak interfaces with crack growth demonstrates behavior characteristic of composites
- Surfaces of the T3 build revealed the extent of process-related underplunge

CHAPTER 4

FSAM BEAM FINITE ELEMENT ANALYSIS

4.1 Introduction

The previous chapters detailed properties of friction stir additively manufactured builds with cast and T3 feedstock materials. However, visualizing the behavior of a full-size fabricated component under load is almost impossible without constructing it, and even then, investigations of the complex internal stress behavior would require further investigation. For this application, nonlinear three-dimensional finite element analysis (FEA) with ANSYS Mechanical 14.0 was chosen to analyze two beams models: one of monolithic 2050-T8 and the other made with the FSAM lap welding process. The behavior of these models could be useful in further understanding this additive process.

4.2 Approach and Model Setup

4.2.1 Material Properties

The thicker/slower/cast build was chosen to populate the FSAM material property data for this analysis, with the beam cross section taken from the weld nugget as shown in Fig. 4.1. The PWHT microhardness results from the previous section were used to approximate local yielding properties within the beam: due to the hardness distributions found with this build, average hardness values were assigned to a total of twenty-five

separate sections. Hardness and yield strength were known for 2050-T3 and 2050-T8, so a linear relationship was used to extrapolate yield strength of the small areas having knowledge of their individual hardness assignments. A diagram of the relationship is shown in Fig. 4.2.

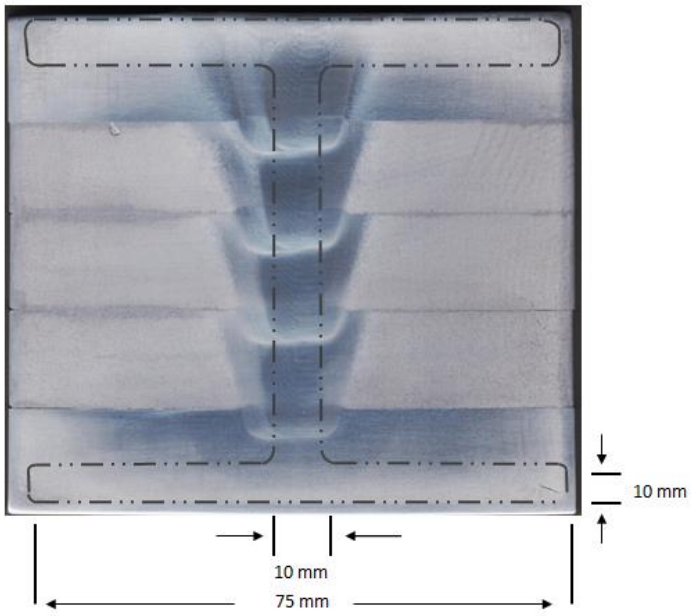

Figure 4.1 Sample beam cross section taken from thicker/slower/cast FSAM build

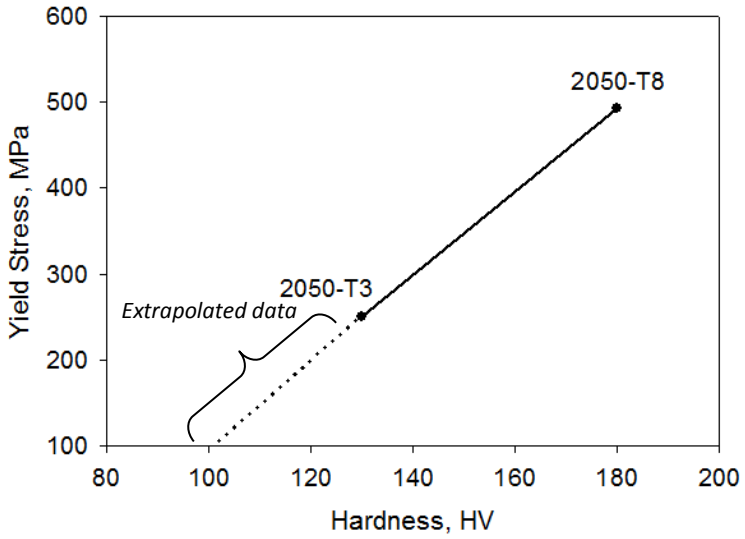

Figure 4.2 Hardness and yield strength relationship for AA2050 tempers

Final sections are displayed in Figure 4.3 below—associated yield strengths are given in Table 4.1. It is noticeable that some of these values are quite low compared to 2050-T3 yield strength of 250 MPa. Material properties of the 2050-T8 beam were determined from tensile tests and results from literature. Displayed in Table 4.2, these values were implemented in the user-defined material properties.

Table 4.1 Yield strength approximations

Section	Est. yield strength MPa
1	283
2	326
3	226
4	180
5	372
6	196
7	409
8	279
9	347
10	196
11	415
12	215
13	202
14	145
15	488
16	434
17	434
18	287
19	287
20	349
21	349
22	299
23	299
24	346
25	346

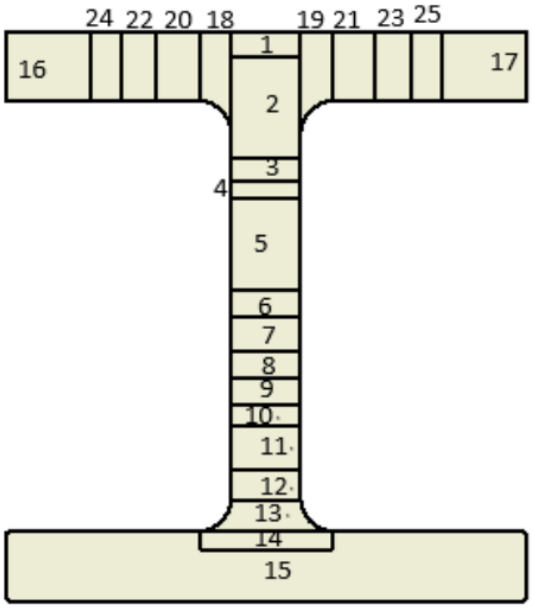

Figure 4.3 Portioned cross sectional areas

Table 4.2 AA2050-T8 Material Properties

Yield strength, MPa	493
Ultimate tensile strength, MPa	540
Young's modulus, GPa	76
Tangent modulus, MPa	787.6

Specifically, the tangent modulus, *ET*, of T8 temper material was determined by the linear relationship between the yield strength and ultimate tensile strength of the material and elongations at these stresses. This is shown in Equation 4.1 below.

$$ET = \frac{\sigma_U - \sigma_Y}{e_U - e_Y} \qquad \textit{Eq. 4.1}$$

4.2.2 Geometry

A simple I-beam cross section was chosen for the test geometry for both models. Shown in Figure 4.4, the width of the flanges was established at 75 mm across. The web and flange thickness were 10 mm, with a total beam length of 500 mm. A moderate radius was applied to the web/flange connection to reduce stress concentration and potential convergence issues arising from sharp edges.

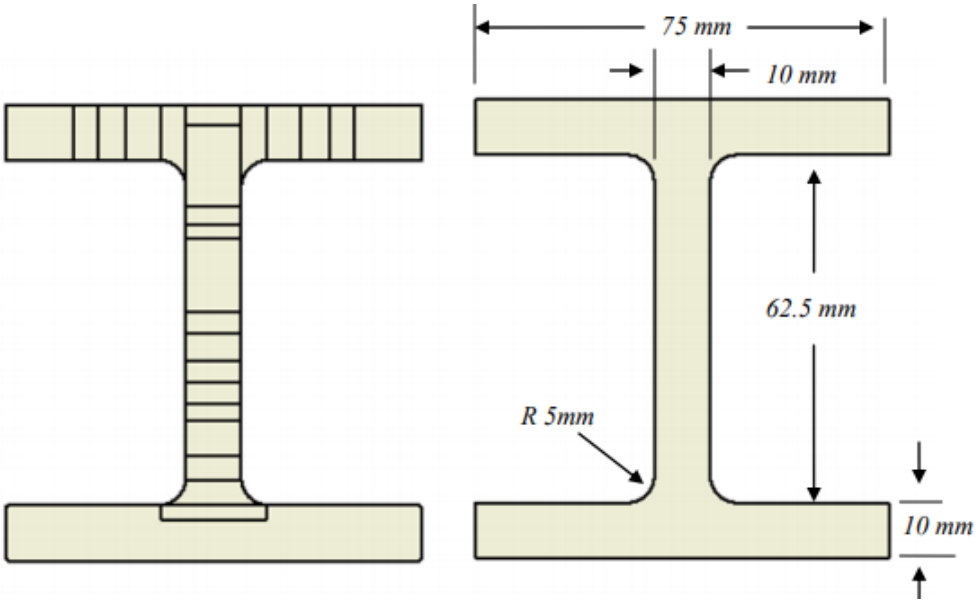

Fig 4.4 Beam cross sectional geometries

4.2.3 Boundary conditions

This analysis was performed as a point-load cantilever beam model. As illustrated in Figure 4.5, one end was given a fixed boundary condition, and the other free end had an applied force. The load within this analysis was determined to be 53 kN, calculated to be beyond the point of outer fiber yielding within a T8 beam with the previously determined material properties. The intent with these loading conditions is to analyze the nonlinear conditions within the beams after the elastic regime.

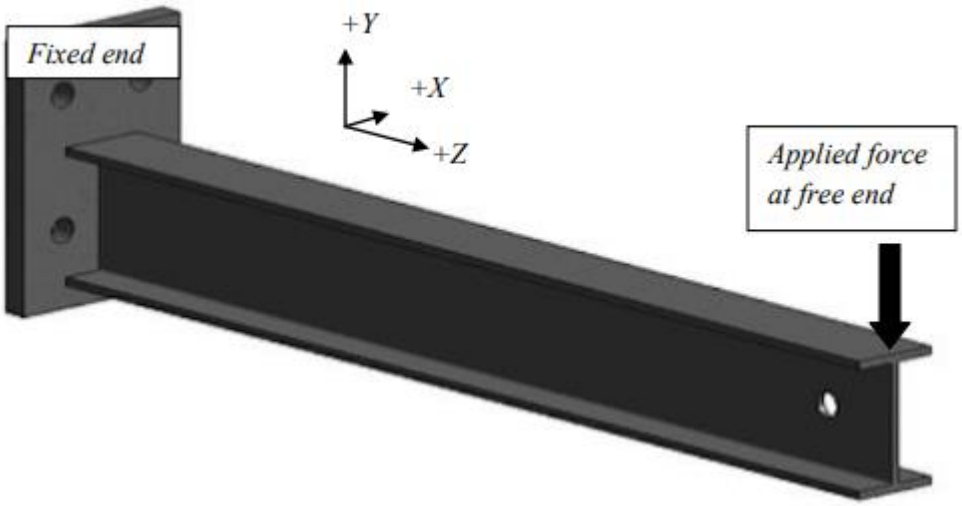

Fig 4.5 Cantilever I-beam system

4.3 Mesh And Refinement

4.3.1 Meshing Method and Convergence

An initial mesh for both beams was given a starting element size of 5 mm, comparable to that shown Figure 4.6 for the FSAM beam. The load and fixed end conditions were applied, and the initial analysis was performed. A variety of test points

were chosen 10 mm from the fixed end of the beams to determine and ensure convergence. The mesh size was decreased to 3 mm shown in Figure 4.7 and the analysis was repeated. It was found that the stress values at these test points had acceptable (<2%) relative error for both models. This is an indication of a converged solution, so the 2050-T8 and FSAM models were determined satisfactory.

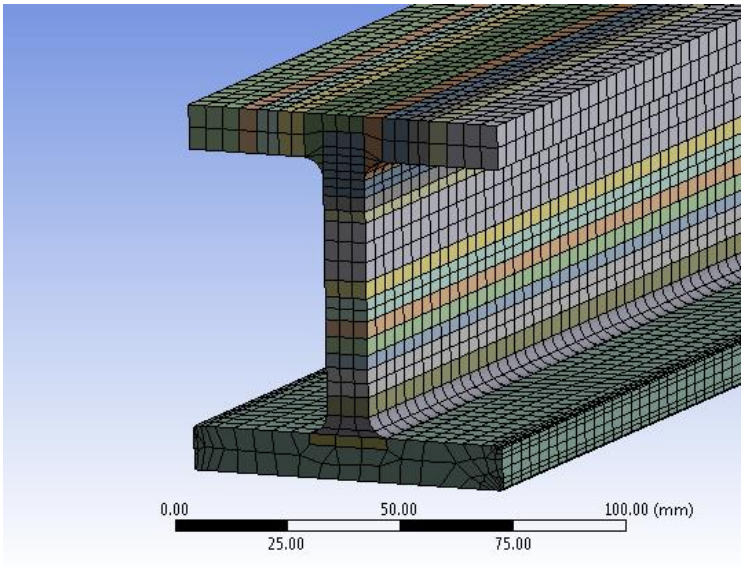

Fig 4.6 Initial 5 mm mesh size shown with FSAM beam

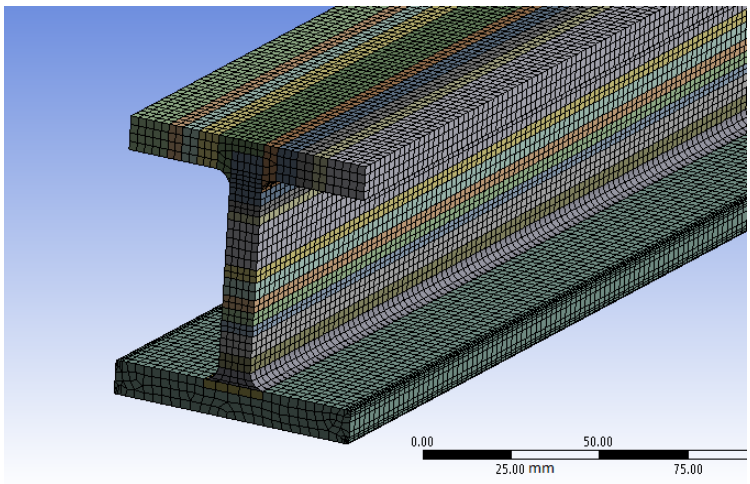

Fig. 4.7 Final 3 mm mesh size

4.3.2 Model Verification

To verify the accuracy of results, the converged 2050-T8 FEA model was evaluated within the linear regime and compared with a linear analytical beam analysis. The equations used for this analysis are shown in Eqns. 4.2 and 4.3 for deflection at the loaded end of the beam, q_p, and bending stress needed to induce yielding of the outer fibers, $\sigma_{bend,Y}$ [42]. The total deflection was a function of beam length, L, applied load, P, second moment of inertia, I_x, and material modulus of elasticity, E. Bend stress required to induce yielding requires the yield moment, M_Y, distance from the centroid to the outer fibers, c, as well as the second moment of inertia. For comparison of analytical solution and ANSYS values, the von Mises distortional energy density yield criterion was used. This states yielding occurs when the von Mises equivalent stress reaches that of the material yield strength.

$$q_p = \int_0^L \frac{Pz^2}{EI_x} \mathrm{d}z = \frac{PL^3}{3EI_x} \qquad \textit{Eq. 4.2}$$

$$\sigma_{bend,Y} = \frac{M_Y c}{I_x} \qquad \textit{Eq. 4.3}$$

$$\textit{Where} \qquad M_Y = -PL$$

At a load of 18.75 kN, total beam deflection and bending stress were found to be within 10% of the calculated values which was satisfactory. Some of the variation between analytical and FEA results could be attributed to the corner radii of the model geometry—this was not applied in the linear calculation.

4.4 Results From Analysis

4.4.1 Initial Loading

At maximum load of 53 kN, both models displayed the total deformation seen in Figures 4.8 and 4.9. The orientation is shown with the fixed end on the left-hand side of the models. The total maximum deformation of the 2050-T8 beam at the point of loading was 14.7 mm, while the weld build resulted in 20.2 mm of max deformation at the loaded beam end. These results show a significant increase of deformation with the FSAM beam compared to that of the monolithic T8 at this load magnitude.

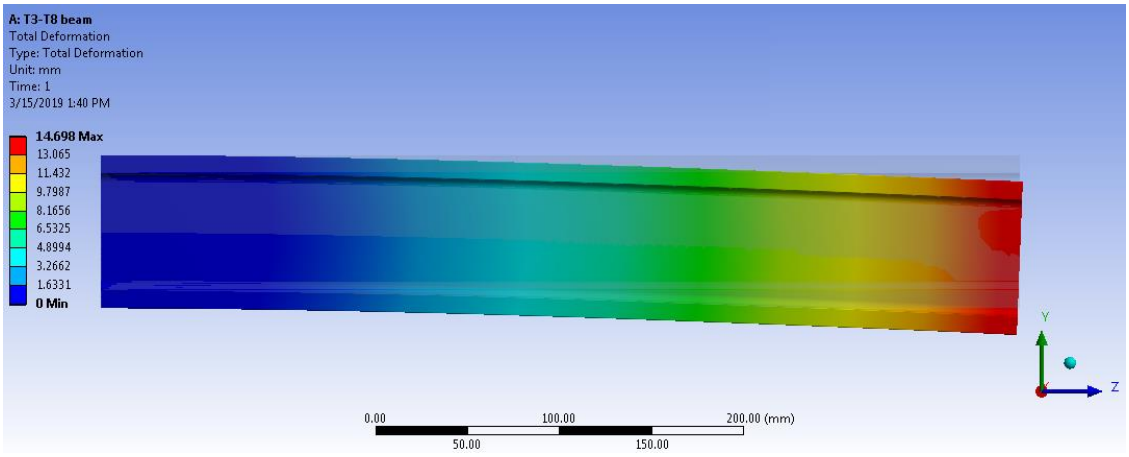

Fig. 4.8 Total deformation of the 2050-T8 model at max load

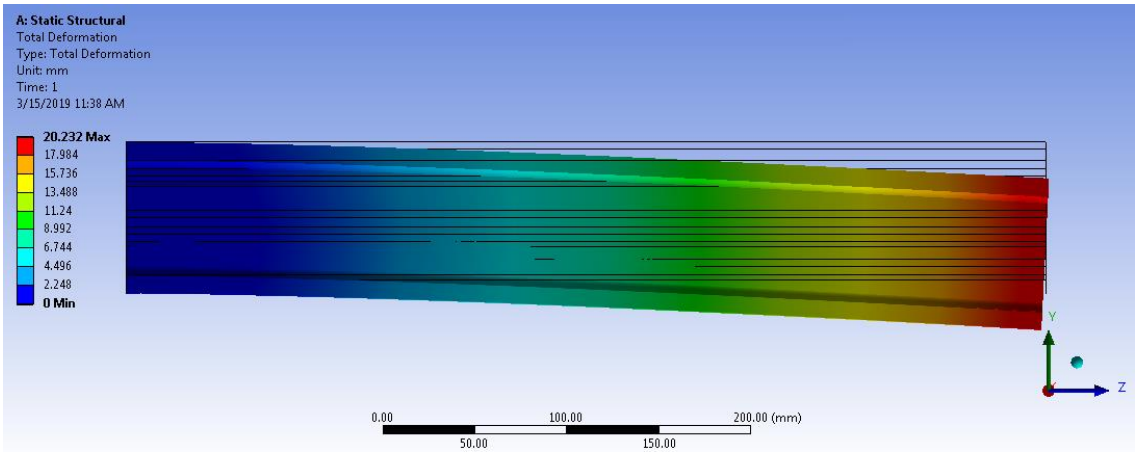

Fig. 4.9 Total deformation of the FSAM model at max load

The von Mises stresses experienced on the fixed end of the models are given on the next page with Figs. 4.11 and 4.12 at the point of maximum loading. The stress concentration is visibly symmetrical for the 2050-T8 model, which is expected. According to the yield criterion, the T8 beam exhibits yielding of the outer fibers and contains various locations past the ultimate tensile strength. However, the FSAM beam cross section shows stress asymmetrical to the centroid, with the largest concentrations on the lower flange. Minimum values were not observed at the centroid likely due to the asymmetry of material properties throughout the flange thickness. Yielding is observed at the outer fibers and further analysis of this model revealed that several sections within the web experienced stress higher than their designated yield strengths. These are captured within the dotted lines of Figure 4.12.

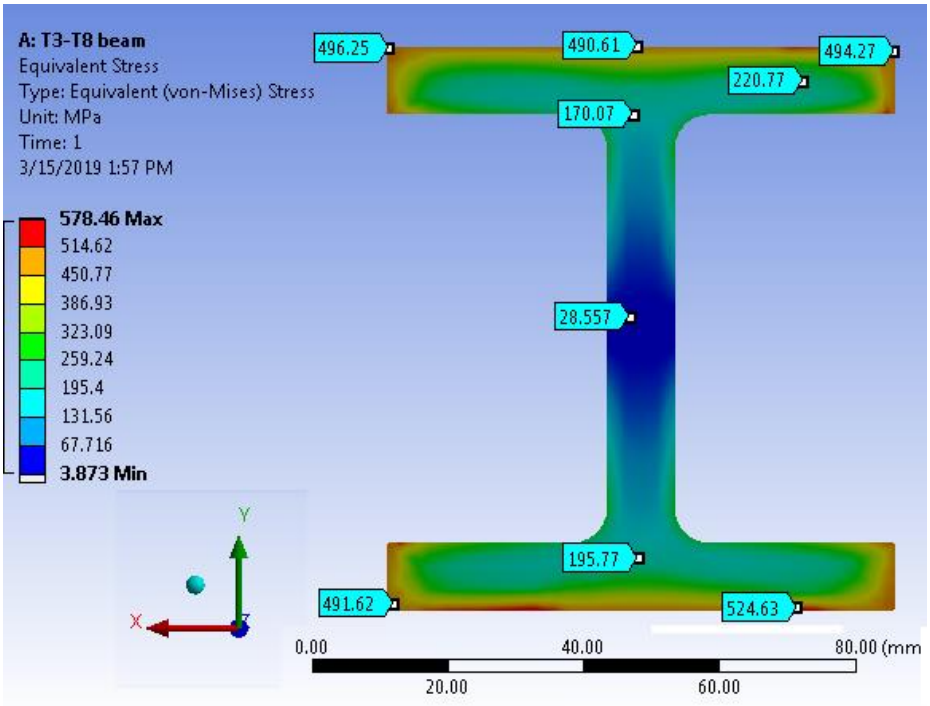

Fig. 4.10 Fixed-end von Mises stresses of the T8 model at max load

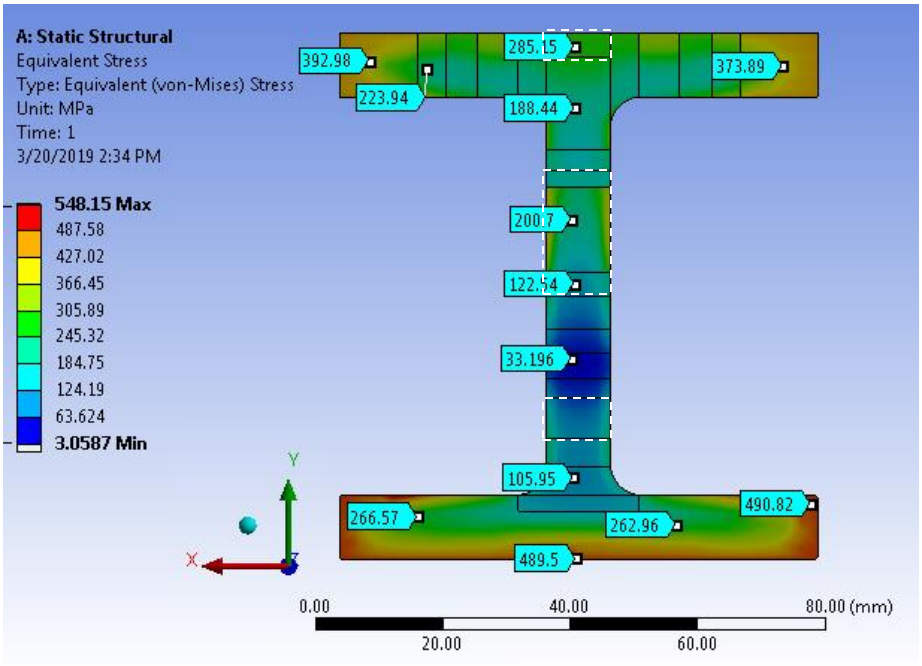

Fig. 4.11 Fixed-end von Mises stresses of the FSAM model at max load

Internal von Mises equivalent stresses for both models were analyzed at test points throughout the cross section at 100 mm from the fixed end as displayed in Figure 4.12. Each test point was placed at 5 mm increments apart. The exact values of stress at the time of maximum loading are given in Table 4.3. The stress distributions for both models are visualized in Figures 4.13 and 4.14.

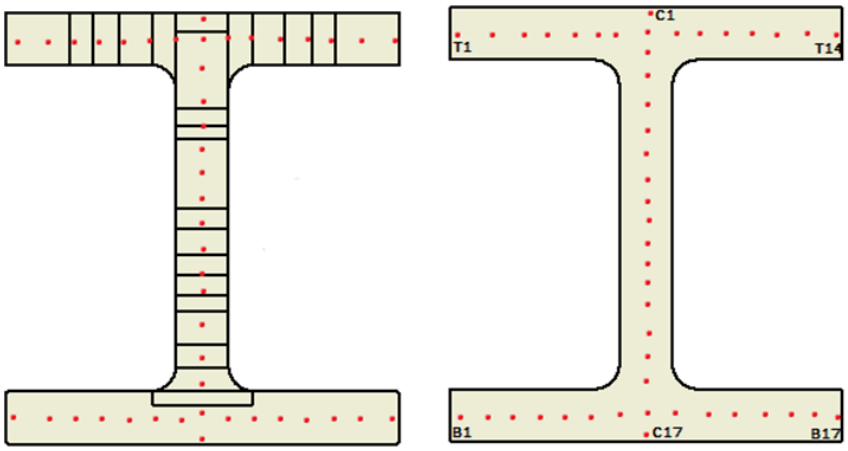

Fig. 4.12 Internal test point locations for both beam models

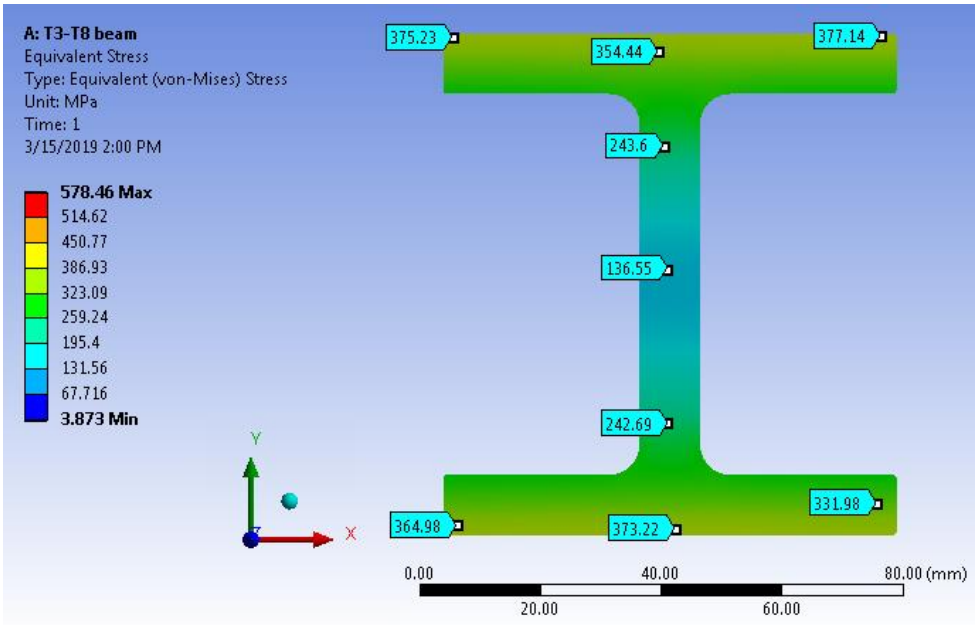

Fig. 4.13 Internal stresses of T8 model 100 mm from fixed end at max load

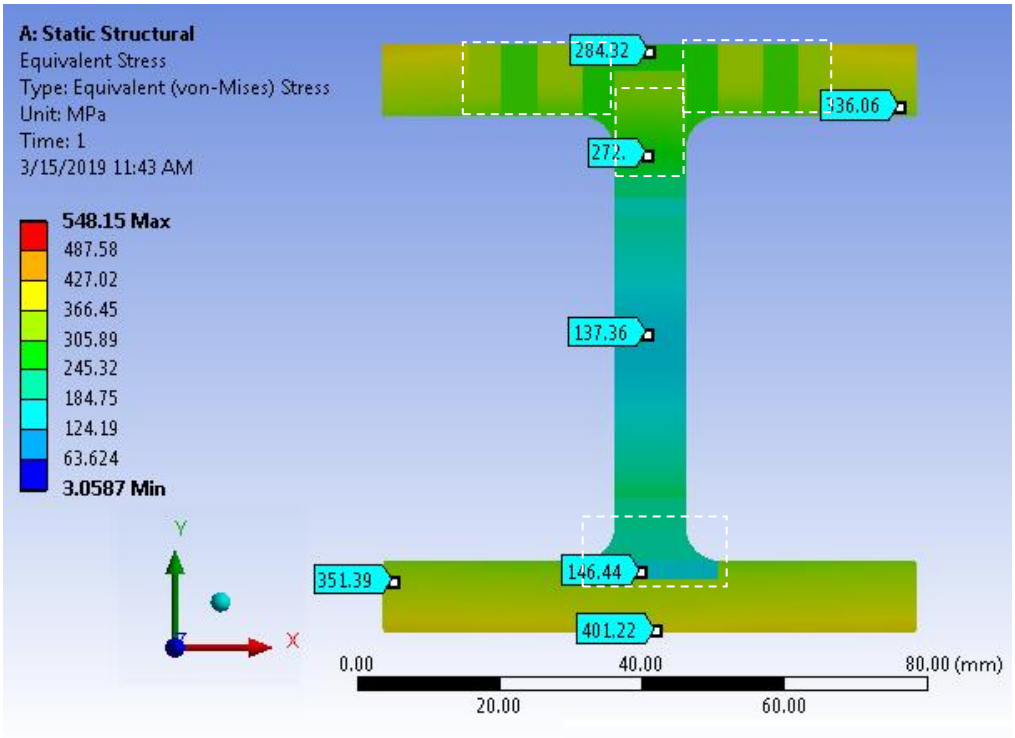

Fig. 4.14 Internal stresses of FSAM model 100 mm from fixed end at max load

Table 4.3 Internal von Mises stresses at test points – maximum load

				Stress, MPa				
Location	FSAM	2050-T8	Location	FSAM	2050-T8	Location	FSAM	2050-T8
T1	370.7	338	*B1*	377.6	339.5	*C1*	284.4	369.7
T2	365.2	338.1	*B2*	376.7	339.7	*C2*	325.7	327.7
T3	346.1	338.4	*B3*	375.6	340.2	*C3*	305.9	292.6
T4	299.5	339	*B4*	374.4	340.8	*C4*	274.3	261.2
T5	344.5	339.8	*B5*	373.2	341.7	*C5*	226.1	225.6
T6	344.2	340.7	*B6*	372.4	342.4	*C6*	202.0	191.7
T7	287.8	340.4	*B7*	369.5	342.7	*C7*	173.5	162.9
T8	325.8	340.4	*B8*	369.5	342.4	*C8*	150.9	142.5
T9	344.2	340.7	*B9*	372.4	342.5	*C9*	138.6	134.5
T10	344.5	339.8	*B10*	373.2	341.7	*C10*	140.4	140.8
T11	299.5	339	*B11*	374.4	340.8	*C11*	157.0	159.9
T12	346.1	338.4	*B12*	375.6	340.2	*C12*	185.0	188
T13	365.1	338.1	*B13*	376.7	339.7	*C13*	220.7	221.6
T14	370.6	338	*B14*	377.6	339.5	*C14*	215.3	256.8
						C15	201.9	228.2
						C16	352.1	324.6
						C17	392.4	369.6

Internally, the T8 beam exhibits symmetrical stress distribution with minimum stress at the centroid and maximums at the outer fibers of the flanges that do not exceed the yield strength. It is evident that the FSAM model experiences higher stresses in the bottom flange compared to the T8 beam. The top flange stress values were shown of a broader spread than the T8 values which were uniform. Several sections shown within the dotted lines of Figure 4.14 were also observed to contain stresses above their assigned yield strengths. These were not only located on the outer flanges, but at the connections between web and flanges.

4.4.2 After Unloading

The models were again analyzed after the maximum load was removed. Final deformations of the two beams after unloading are given in Figures 4.15 and 4.16. The T8 beam appears to have almost no final deformation as a result of this load/unload cycle. However, the FSAM beam results in a final plastic deformation of 5.4 mm. This is further explored in the load-deformation plot of Figure 4.17. With this applied load, the FSAM beam exhibits the largest deformation in both the loading and unloaded steps with considerable plastic deformation. However, the T8 beam remains almost elastic with a final deformation of 0.0094 mm

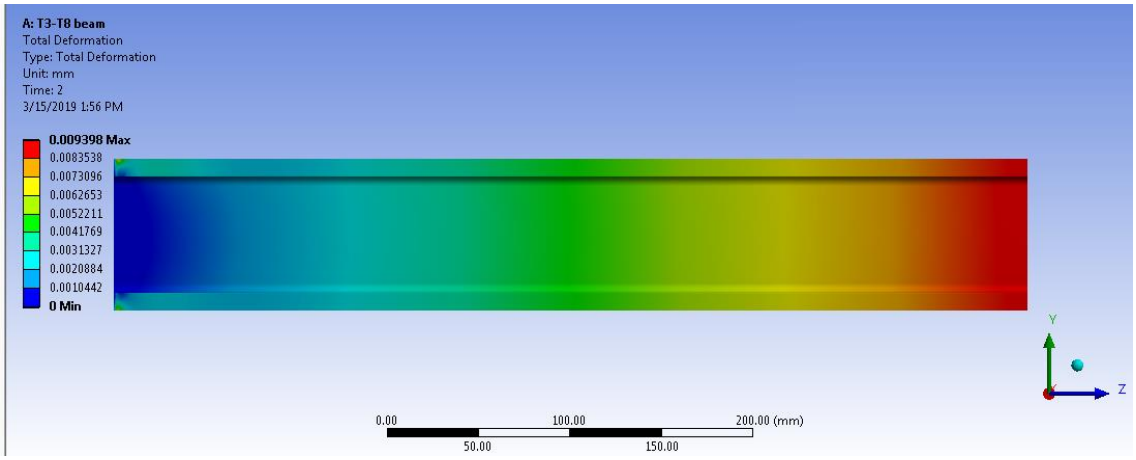

Fig. 4.15 AA2050-T8 beam model final deformation

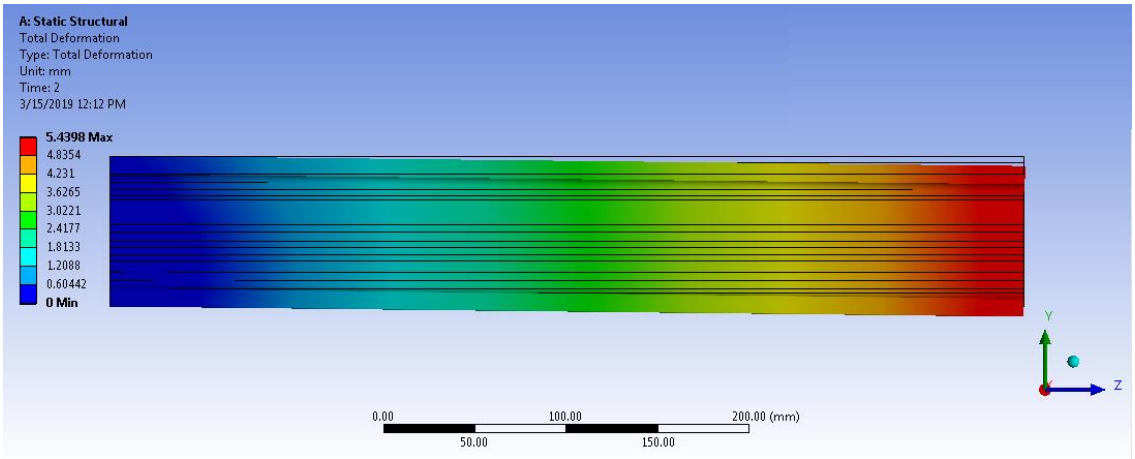

Fig. 4.16 FSAM beam model final deformation

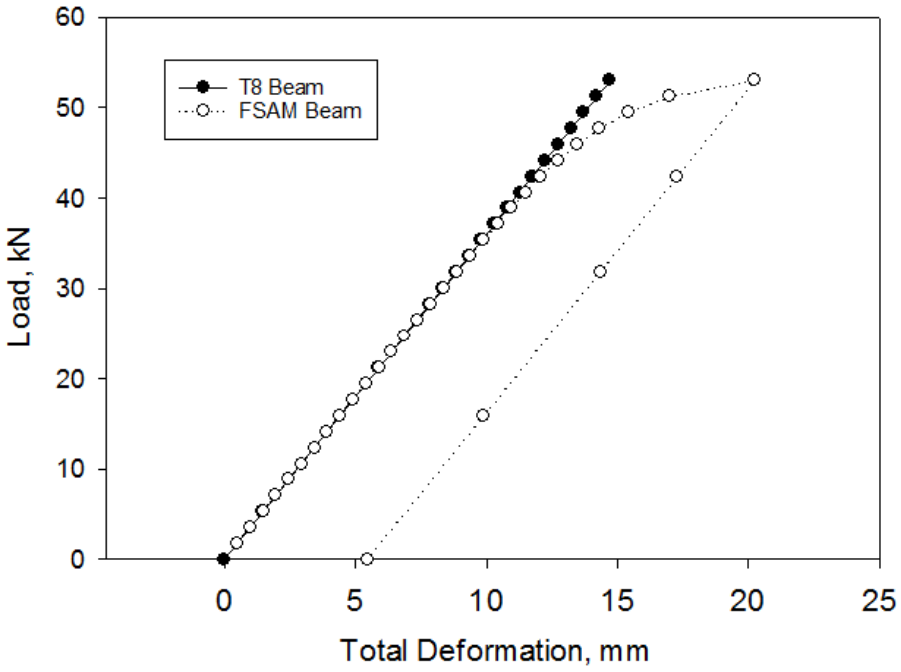

Fig. 4.17 Load-deformation behavior of both beam models

Residual von Mises stresses at the fixed end cross sections are shown in Figures 4.18 and 4.19 on the next page. Concentrated stress is observed at the corners of both builds however this could partially be caused by sharp edges of the geometry at these locations. The stress at these points also does not exceed the yield strength of the material. The T8 model does retain small amounts of stress after unloading, but not to the degree of the FSAM beam. Many sections within the welded build contain considerable amounts of residual stress. Sections 18 and 19 of the top flange experience concentrations at the outer fibers that are above their respective yield strengths.

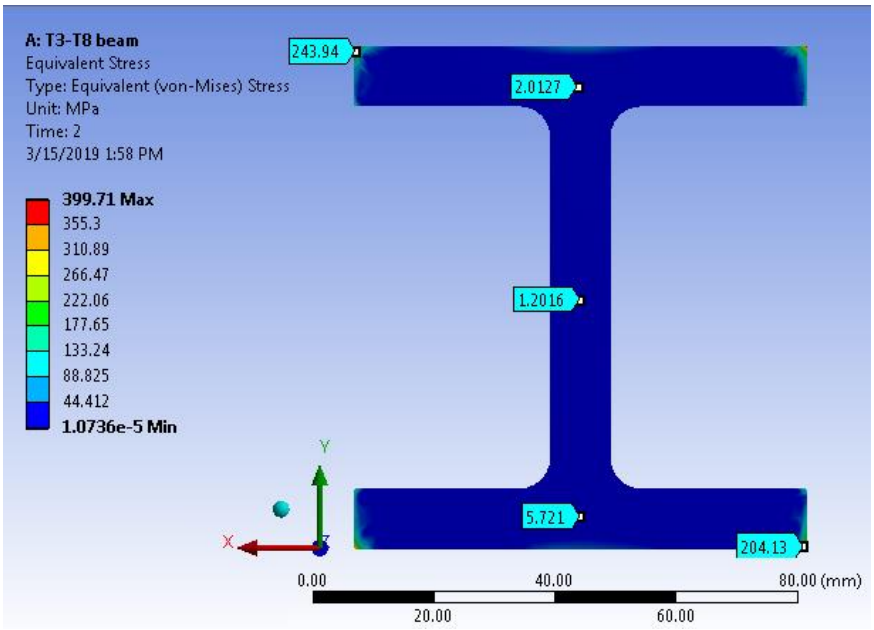

Fig. 4.18 Residual stress at the fixed end of the T8 beam model

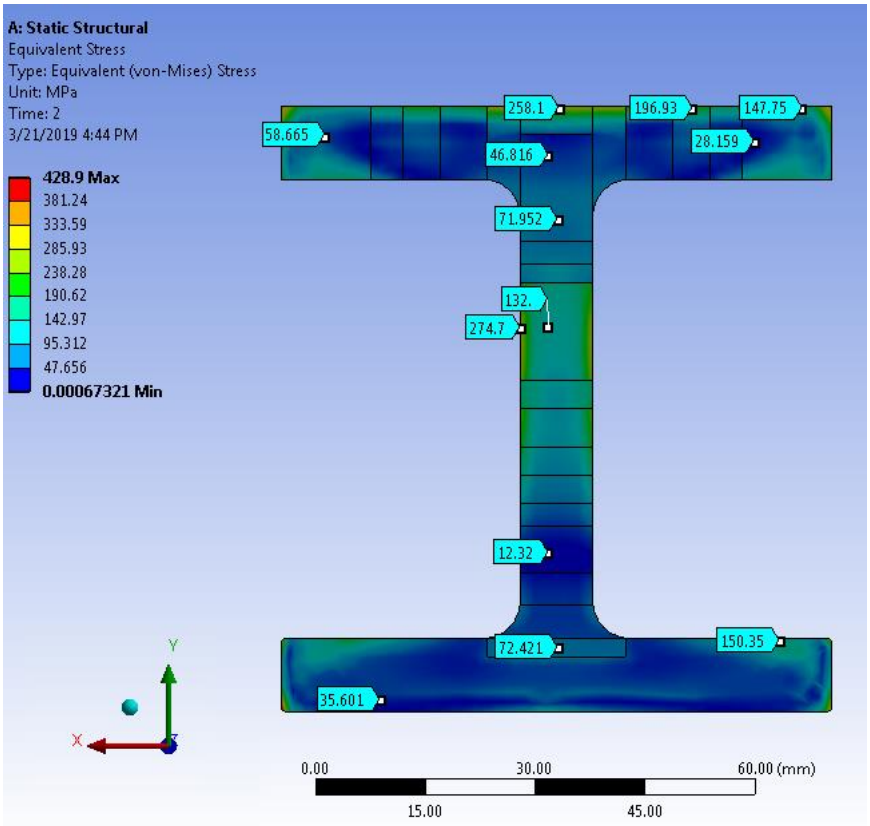

Fig. 4.19 Residual stress at the fixed end of the FSAM model

Internal residual stress at 100 mm from the fixed end can be observed in Figures 4.20 and 4.21 and also further analyzed at the test points in Table 4.4. Some residual stresses are observed with the 2050-T8 beam, but they are minimal. It is evident that internally, stresses remain within many sections of the welded beam at this location from the fixed end. Most importantly, the stress observed at the base of the web in section 14 exceeds the yield strengths of this section due to the assigned properties of this location. The T8 model in comparison contains negligible residual internal stress at the time of unloading.

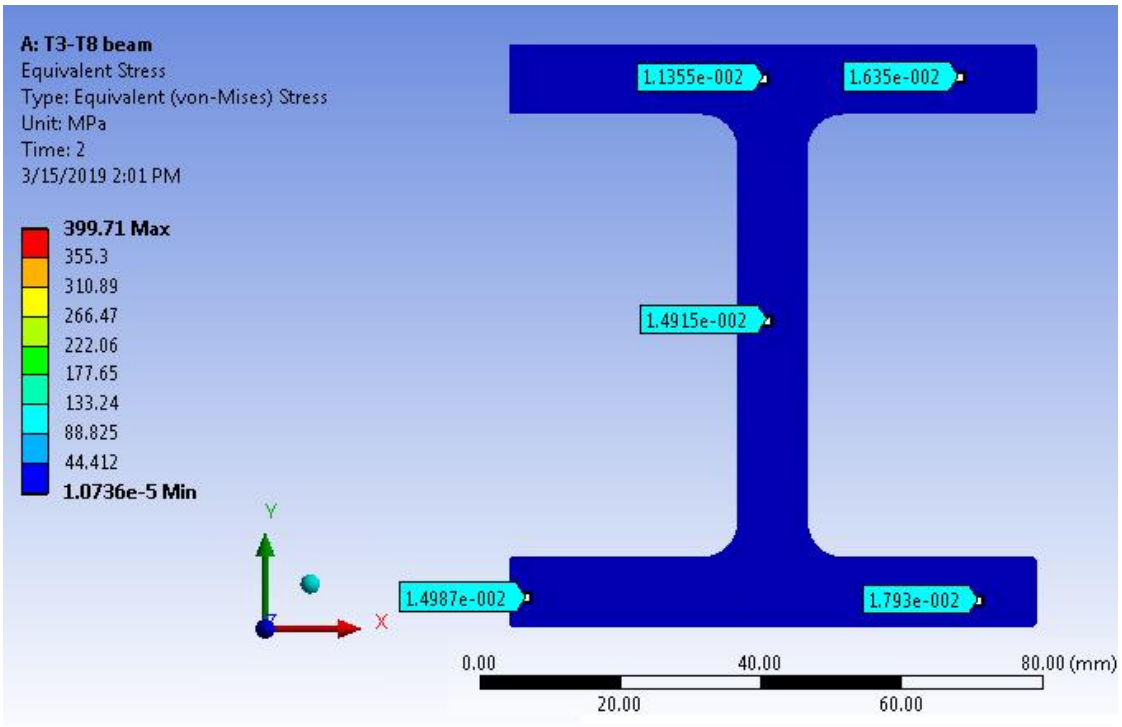

Fig. 4.20 Internal stresses of the T8 model after unloading

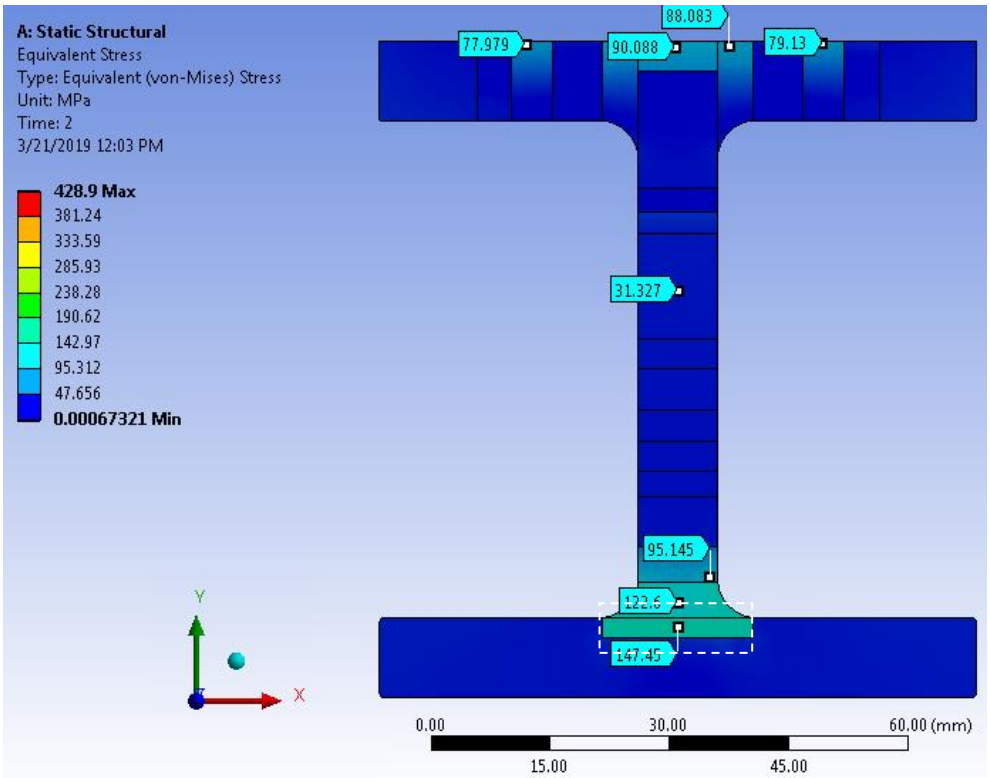

Fig. 4.21 Internal stresses of the FSAM model after unloading

Table 4.4 Internal von Mises stresses at test points –Unloaded

				Stress, MPa				
Location	FSAM	2050-T8	Location	FSAM	2050-T8	Location	FSAM	2050-T8
T1	37.6	0.017	*B1*	34.7	0.015	*C1*	94.0	0.019
T2	34.2	0.012	*B2*	34.2	0.010	*C2*	17.4	0.016
T3	22.5	0.017	*B3*	33.5	0.014	*C3*	25.3	0.022
T4	40.1	0.018	*B4*	32.9	0.015	*C4*	31.2	0.015
T5	11.5	0.019	*B5*	32.4	0.015	*C5*	26.6	0.016
T6	9.0	0.020	*B6*	34.2	0.014	*C6*	35.3	0.016
T7	16.6	0.018	*B7*	32.5	0.014	*C7*	34.8	0.015
T8	16.6	0.018	*B8*	32.4	0.011	*C8*	34.0	0.015
T9	9.0	0.020	*B9*	34.1	0.014	*C9*	33.4	0.015
T10	11.5	0.018	*B10*	32.4	0.013	*C10*	32.8	0.014
T11	40.1	0.017	*B11*	32.9	0.013	*C11*	32.4	0.014
T12	22.5	0.016	*B12*	33.5	0.013	*C12*	32.0	0.013
T13	34.2	0.011	*B13*	34.2	0.013	*C13*	31.8	0.013
T14	37.6	0.013	*B14*	34.7	0.014	*C14*	83.6	0.013
						C15	128.8	0.016
						C16	36.7	0.012
						C17	21.8	0.021

4.5 Conclusions

Mechanical properties of a friction stir additive manufacturing build were used to populate a FEA beam model and compared to an identical beam made from 2050-T8. The FSAM model properties were determined by grouping sections of similar microhardness and then assigned corresponding yield strengths assuming AA2050 temper property relationships.

With the same load and geometry, the welded beam showed significant residual stress and plastic deformation as a result of the loading and unloading cycles. Importantly, after the load was removed some of the sections within the beam and away from the fixed end experienced residual stresses above their assigned yield strengths. However, the T8 beam did not exhibit severe plastic deformation or major residual stresses.

CHAPTER 5

CONCLUSIONS

1. The use of opposing, double weld passes is an effective strategy to reduce the retreating side CLD in friction stir lap welds

2. Resulting inhomogeneous hardness distribution of FSAM builds with this aluminum alloy creates areas of lower strength which do not recover with the applied PWHT.
    a. Strain concentrates, and eventual failure occurs at these low-hardness areas under tensile load

3. Fracture behavior of FSAM is much like that of a composite—There is a noticeable relationship of crack growth orientation with respect to welding direction/lap layers as a result of the inhomogeneous hardness distributions

4. There is not a significant disadvantage to using cast AA2050 feedstock with the FSAM process compared to the use of AA2050-T3

5. From the current investigations at this point, this AM process is not well suited to industrial applications intending to replace wrought materials such as AA2050-T3 or AA2050-T8. Further exploration is required with this process to explore its potential technology readiness.

CHAPTER 6

FUTURE RECOMMENDATIONS

1. Microstructural characterization of the FSAM materials could be performed to examine grain size and precipitate phases throughout in order to further explore the properties of friction stir lap welded additive manufacturing with the current alloy or investigate other alloys for their FSAM potential.

2. It may also be prudent to investigate alternative heat treatments or explore aging times for FSAM hardness recovery with AA2050.

3. Determine local yield strengths from DIC tensile results, and assign these to the FEA model sections for more accurate analysis

4. Conduct in-depth fractography and characterization of tensile and fracture test surfaces to investigate the mechanics of the current build failures

5. Perform a cost-benefit analysis of FSAM compared to other additive processes and current industry methods involving subtractive manufacturing

REFERENCES

[1] Mishra, R. S., & Mahoney, M. W. (2007). Introduction. In Mishra, R. S., & Mahoney, M. W. (Eds.) *Friction Stir Welding and Processing*. (pp. 1-5). Materials Park, OH: ASM International.

[2] Threadgill, P. L., Leonard, A. J., Shercliff, H. R., & Withers, P. J. (2009). Friction stir welding of aluminium alloys. *International Materials Review*, *54*(2), 49–93. https://doi.org/10.1179/174328009X411136

[3] Tang, W & Guo, X & Mcclure, John & Murr, Lawrence & Nunes, A.C.. (1998). Heat Input and Temperature Distribution in Friction Stir Welding. *Journal of Materials Processing & Manufacturing Science, 7*, 163-172. 10.1106/55TF-PF2G-JBH2-1Q2B.

[4] Reynolds, A.P. (2007). Microstructure development in aluminum alloy friction stir welds. In Mishra, R. S., & Mahoney, M. W. (Eds.) *Friction Stir Welding and Processing*. (pp. 51-70). Materials Park, OH: ASM International.

[5] Khodabakhshi, F., & Gerlich, A. P. (2018, December 1). Potentials and strategies of solid-state additive friction-stir manufacturing technology: A critical review. *Journal of Manufacturing Processes*. Elsevier Ltd.

[6] Baumann, J. A. (2012). Final Technical Report - Production of Energy Efficient Preform Structures (PEEPS). United States Department of Energy.

[7] Cruz, J. (2016). Does Friction Stir Welding Add Up ? *Edison Welding Institute*.

[8] Palanivel, S., Sidhar, H., & Mishra, R. S. (2015). Friction Stir Additive Manufacturing: Route to High Structural Performance. *JOM*, *67*(3), 616–621. https://doi.org/10.1007/s11837-014-1271-x

[9] Buffa, G., Campanile, G., Fratini, L., & Prisco, A. (2009). Friction stir welding of lap joints: Influence of process parameters on the metallurgical and mechanical properties. *Materials Science and Engineering A*, *519*(1–2), 19–26.

[10] Schneider, J.A. (2007). Temperature distribution and resulting metal flow. In Mishra, R. S., & Mahoney, M. W. (Eds.) *Friction Stir Welding and Processing*. (pp. 37-49). Materials Park, OH: ASM International.

[11] Babu, S., Sankar, V. S., Janaki Ram, G. D., Venkitakrishnan, P. V., Madhusudhan Reddy, G., & Prasad Rao, K. (2012). Microstructures and mechanical properties of friction stir lap welded aluminum alloy AA2014. *Journal of Materials Science and Technology*, *28*(5), 414–426. https://doi.org/10.1016/S1005-0302(12)60077-2

[12] Liu, H., Hu, Y., Peng, Y., Dou, C., & Wang, Z. (2016). The effect of interface defect on mechanical properties and its formation mechanism in friction stir lap welded joints of aluminum alloys. *Journal of Materials Processing Technology*, *238*, 244–254. https://doi.org/10.1016/j.jmatprotec.2016.06.029

[13] Shirazi, H., Kheirandish, S., & Safarkhanian, M. A. (2015). Effect of process parameters on the macrostructure and defect formation in friction stir lap welding of AA5456 aluminum alloy. *Measurement: Journal of the International Measurement Confederation*, *76*, 62–69.

[14] Fersini, D., & Pirondi, A. (2007). Fatigue behaviour of Al2024-T3 friction stir welded lap joints. *EngineeringFracture Mechanics*, *74*(4), 468–480. https://doi.org/10.1016/j.engfracmech.2006.07.010

[15] Yuqing, M., Liming, K., Chunping, H., Fencheng, L., & Qiang, L. (2016). Formation characteristic, microstructure, and mechanical performances of aluminum-based components by friction stir additive manufacturing. *International Journal of Advanced Manufacturing Technology*, *83*(9–12), 1637–1647. https://doi.org/10.1007/s00170-015-7695-9.

[16] Cao, X., & Jahazi, M. (2009). Effect of welding speed on lap joint quality of friction stir welded AZ31 magnesium alloy. In *ASM Proceedings of the International Conference: Trends in Welding Research* (pp. 72–80). https://doi.org/10.1361/cp2008twr072

[17] Aldanondo, E., Arruti, E., & Echeverria, A. (2017). Friction Stir Weld Lap Joint Properties in Aeronautic Aluminium Alloys. In Y. Hovanski, R. Mishra, Y. Sato, P. Upadhyay, & D. Yan (Eds.), *Friction Stir Welding and Processing IX* (pp. 109–117). Cham: Springer International Publishing. https://doi.org/10.1007/978-3-319-52383-5_12

[18] Cederqvist, L., & Reynolds, A. P. (2001). Factors Affecting the Properties of Friction Stir Welded Aluminum Lap Joints. *Welding Journal*, *80*(12), 281–287.

[19] Ericsson, M., Jin, L. Z., & Sandström, R. (2007). Fatigue properties of friction stir overlap welds. *International Journal of Fatigue*, *29*(1), 57–68.

[20] Song, Y., Yang, X., Cui, L., Hou, X., Shen, Z., & Xu, Y. (2014). Defect features and mechanical properties of friction stir lap welded dissimilar AA2024-AA7075

aluminum alloy sheets. *Materials and Design*, *55*, 9–18. https://doi.org/10.1016/j.matdes.2013.09.062

[21] Thomas, W. M., Johnson, K. I., & Wiesner, C. S. (2003). Friction stir welding-recent developments in tool and process technologies. *Advanced Engineering Materials*, *5*(7), 485–490. https://doi.org/10.1002/adem.200300355

[22] Dubourg, L., Merati, A., & Jahazi, M. (2010). Process optimisation and mechanical properties of friction stir lap welds of 7075-T6 stringers on 2024-T3 skin. *Materials and Design*, *31*(7), 3324–3330.

[23] Meng, X., Xu, Z., Huang, Y., Xie, Y., Wang, Y., Wan, L., Cao, J. (2018). Interface characteristic and tensile property of friction stir lap welding of dissimilar aircraft 2060-T8 and 2099-T83 Al–Li alloys. *International Journal of Advanced Manufacturing Technology*, *94*(1–4), 1253–1261.

[24] Arbegast, W., J. (2007) Application of Friction Stir Welding and Related Technologies. In Mishra, R. S., & Mahoney, M. W. (Eds.) *Friction Stir Welding and Processing*. (pp. 273-308). Materials Park, OH: ASM International.

[25] Lequeu, P., Smith, K. P., & Daniélou, A. (2010). Aluminum-copper-lithium alloy 2050 developed for medium to thick plate. *Journal of Materials Engineering and Performance*, *19*(6), 841–847. https://doi.org/10.1007/s11665-009-9554-z

[26] James, R. S. (1990) Aluminum-Lithium Alloys. In *ASM Handbook (*Vol. 2, pp. 178-199*)*. https://doi.org/10.31399/asm.hb.v02.a0001063

[27] Warner, T., Sigli, C., Gasqueres, C., & Danielou, A. (2011). *U.S. Patent No. US20110209801A2*. Washington, DC: U.S. Patent and Trademark Office.

[28] Colvin, E. L., Rioja, R. J., Yocum, L. A., & Denzer, D. K. (2009). *U.S. Patent No. US20090142222A1*. Washington, DC: U.S. Patent and Trademark Office.

[29] Sidhar, H., Mishra, R. S., Reynolds, A. P., & Baumann, J. A. (2017). Impact of thermal management on post weld heat treatment efficacy in friction stir welded 2050-T3 alloy. *Journal of Alloys and Compounds*, *722*, 330–338.

[30] Malard, B., De Geuser, F., & Deschamps, A. (2015). Microstructure distribution in an AA2050 T34 friction stir weld and its evolution during post-welding heat treatment. *Acta Materialia*, *101*, 90–100.

[31] Hfaiedh, N., Peyre, P., Song, H., Popa, I., Ji, V., & Vignal, V. (2015). Finite element analysis of laser shock peening of 2050-T8 aluminum alloy. *International Journal of Fatigue*, *70*, 480–489. https://doi.org/10.1016/j.ijfatigue.2014.05.015

[32] Baffari, D. (2019, March 6). E-mail correspondence.

[33] Pouget, G., & Reynolds, A. P. (2008). Residual stress and microstructure effects on fatigue crack growth in AA2050 friction stir welds. International Journal of Fatigue, 30(3), 463–472. https://doi.org/10.1016/j.ijfatigue.2007.04.016

[34] De Geuser, F., Malard, B., & Deschamps, A. (2014). Microstructure mapping of a friction stir welded AA2050 Al-Li-Cu in the T8 state. *Philosophical Magazine*, *94*(13), 1451–1462. https://doi.org/10.1080/14786435.2014.887862

[35] Dhondt, M., Aubert, I., Saintier, N., & Olive, J. M. (2015). Mechanical behavior of periodical microstructure induced by friction stir welding on Al-Cu-Li 2050 alloy. *Materials Science and Engineering A*, *644*, 69–75.

[36] Avettand-Fènoël, M. N., & Taillard, R. (2016). Effect of a pre or postweld heat treatment on microstructure and mechanical properties of an AA2050 weld obtained by SSFSW. *Materials and Design*, *89*, 348–361.

[37] Avettand-Fenoel, M. N., & Taillard, R. (2015). Heterogeneity of the Nugget Microstructure in a Thick 2050 Al Friction-Stirred Weld. *Metallurgical and Materials Transactions A: Physical Metallurgy and Materials Science*, *46*(1), 300–314. https://doi.org/10.1007/s11661-014-2638-x

[38] ASTM E1820-18ae1, Standard Test Method for Measurement of Fracture Toughness, ASTM International, West Conshohocken, PA, 2018

[39] Brown, R. (2008). Multi-pass friction stir welding of AA2195 and AA7050: Effects on microstructure, mechanical properties and process response variables (Master's Thesis).

[40] Soni, N. and Chandrashekhar, S. (2016). Defects formation in friction stir welding: a review. *National Symposium of Mechanical Engineering Research Scholar (NSMERS-2016.)* DOI: 10.13140/RG.2.2.19381.93921.

[41] Hafley, R. A., Domack, M. S., Hales, S. J., & Shenoy, R. N. (2011). Evaluation of Aluminum Alloy 2050-T84 Microstructure and Mechanical Properties as Ambient and Cryogenic Temperatures. *National Aeronautics and Space Administration*, 23681–2199.

[42] Boresi, A. P. & Schmidt, R. J. (2005). *Advanced Mechanics of Materials*. 6th ed. John Wiley & Sons, Inc.

APPENDIX A

25 MM PIN DIMENSIONS

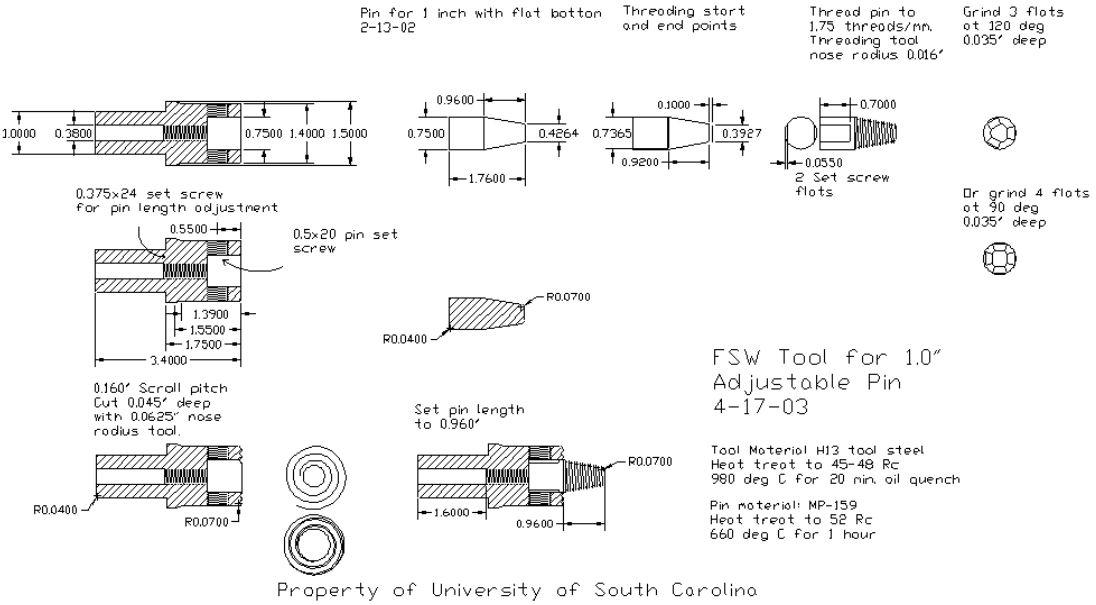

APPENDIX B

12.85 MM PIN DIMENSIONS

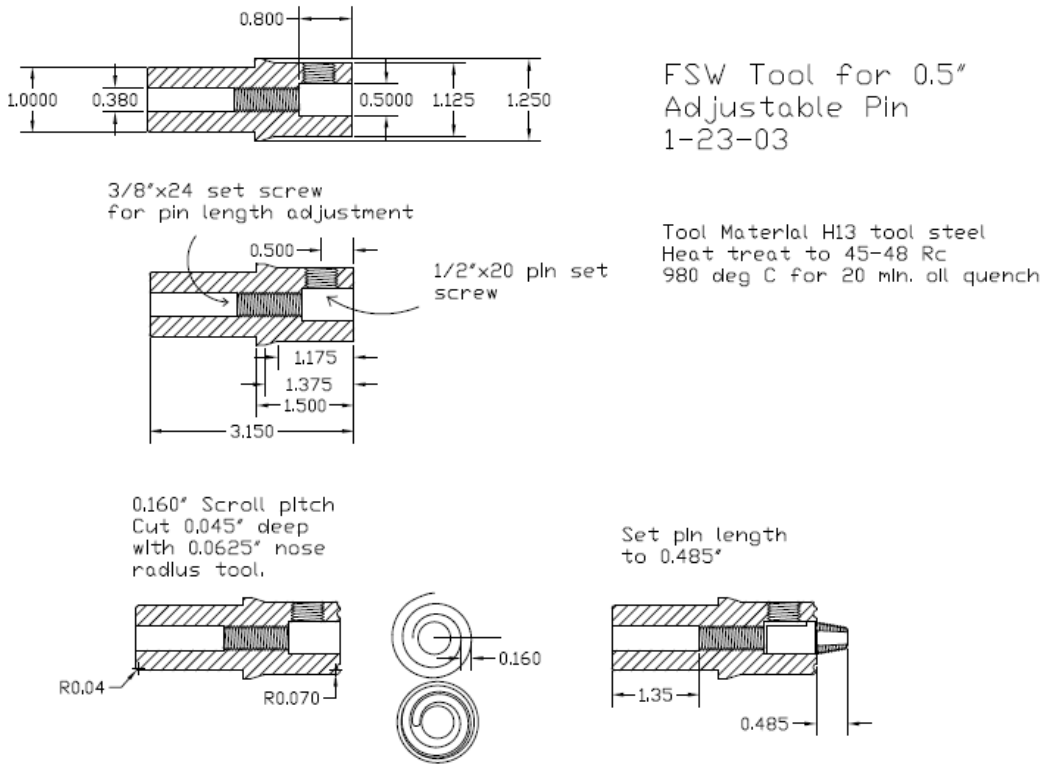

APPENDIX C

TENSILE SAMPLE GEOMETRY

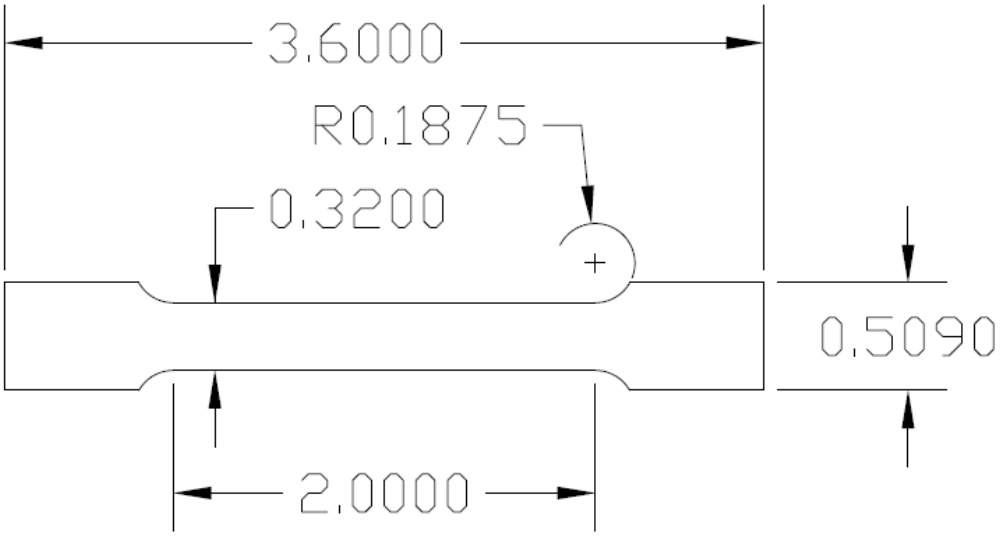

APPENDIX D

COMPACT TENSION COUPON GEOMETRY

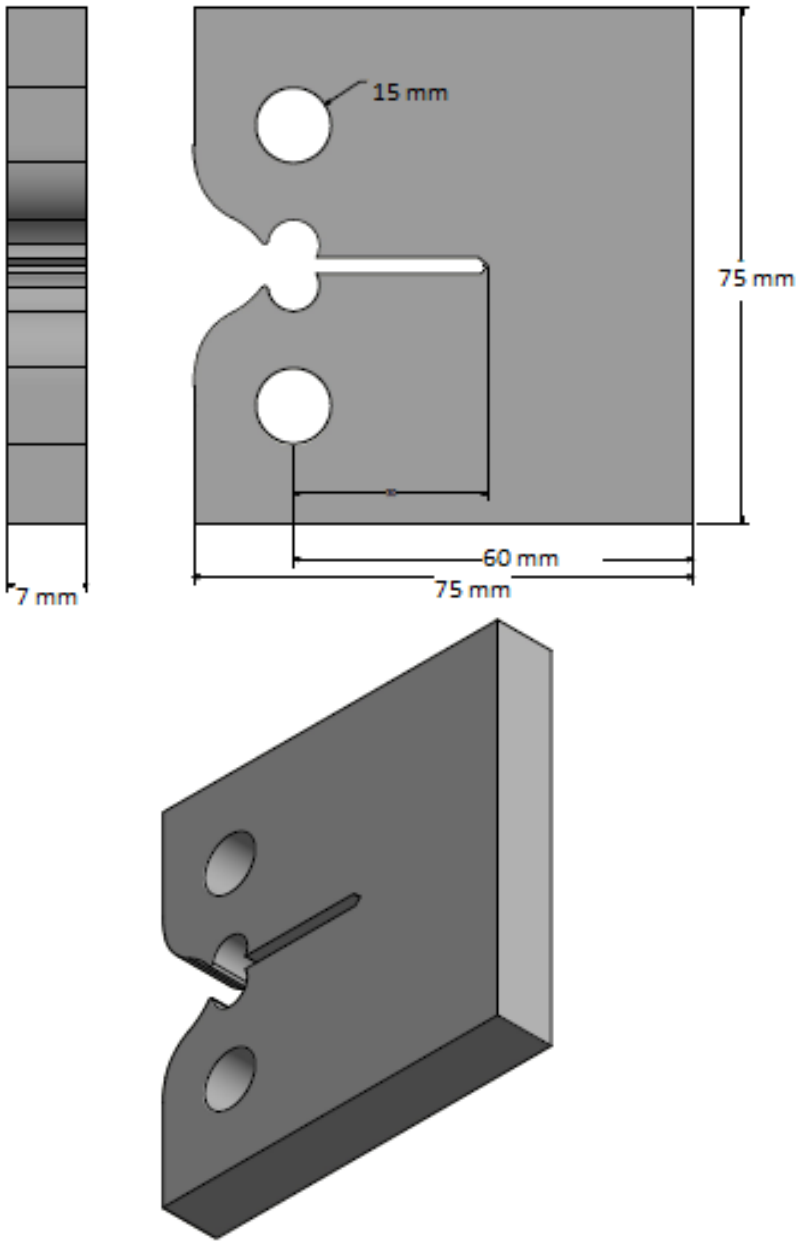

APPENDIX E

WELD PROCESS FEEDBACK OF THICKER/SLOWER/CAST BUILD

Layer - pass	X Force (lb_f)	Y Force (lb_f)	Z Force (lb_f)	Steady State Temp (°C)	Max Temp (°C)	Torque (N-m)	Power (kW)
Layer 1-1	1,723	3,564	12,002	501	512	373	7.8
Layer 1-2	2,400	3,964	12,000	517	531	382	8
Layer 2-1	1,694	3,927	12,002	503	522	371	7.8
Layer 2-2	2,071	3,678	12,004	519	527	383	8
Layer 3-1	1,634	3,192	12,001	506	554	384	8
Layer 3-2	2,303	4,196	12,007	515	525	387	8.1
Layer 4 - 1 *2050-T3*	2,373	2,829	12,000	540	556	383	8
Layer 4-2 *2050-T3*	2,171	3,618	12,001	527	531	396	8.3

APPENDIX F

WELD PROCESS FEEDBACK OF THINNER/FASTER/CAST BUILD

Layer- weld pass	X Force (lb_f)	Y Force (lb_f)	Z Force (lb_f)	Steady State Temp (°C)	Max Temp (°C)	Torque (N-m)	Power, kW
Layer 1-1	896	1216	7000	483	511	167	4.4
Layer 1-2	897	1423	7000	487	505	162	4.2
Layer 2-1	780	1212	7000	481	501	164	4.3
Layer 2-2	1011	1323	7000	490	501	163	4.3
Layer 3-1	809	1241	7000	480	498	170	4.5
Layer 3-2	816	1433	7000	487	501	168	4.4
Layer 4 -1	889	1218	6999	483	505	164	4.3
Layer 4-2	939	1400	6999	490	512	162	4.2
Layer 5-1	729	1183	6999	486	502	161	4.2
Layer 5-2	788	1382	7000	492	503	160	4.2
Layer 6-1	657	1277	7000	483	496	167	4.4
Layer 6-2	1164	1436	7000	491	497	164	4.3
Layer 7-1 *(2050-T3)*	1656	2290	6999	480	514	155	4.1
Layer 7-2 *(2050-T3)*	1028	1456	6999	497	503	165	4.3

APPENDIX G

WELD PROCESS FEEDBACK OF THINNER/FASTER/T3 BUILD

Layer- weld pass	X Force (lb_f)	Y Force (lb_f)	Z Force (lb_f)	Steady State Temp (°C)	Max Temp (°C)	Torque (N-m)	Power, kW
Layer 1-1	1557	1747	7501	493	508	170.3	4.5
Layer 1-2	1116	1111	7501	496	503	178.8	4.7
Layer 2-1	1656	2060	7499	488	503	161.4	4.2
Layer 2-2	840	994	7499	500	507	169.7	4.4
Layer 3-1	1388	1961	7500	488	501	160.1	4.2
Layer 3-2	776	987	7500	499	506	168.2	4.4
Layer 4 -1	1462	2084	7500	488	509	159.2	4.2
Layer 4-2	940	1000	7499	499	509	168.4	4.4
Layer 5-1	1503	2176	7501	483	502	165.0	4.3
Layer 5-2	908	995	7499	498	508	171.2	4.5
Layer 6-1	1499	2237	7500	485	501	160.2	4.2
Layer 6-2	961	1058	7500	499	506	168.1	4.4
Layer 7-1	1463	2193	7501	489	505	157.8	4.3
Layer 7-2	930	1023	7499	502	506	166	4.4